AN ABSTRACT OF THE THESIS OF

Rainer Schwenker for the degree of Master of Science in Physics
presented on December 3, 1990.

Title : Perturbed Angular Correlation Spectroscopy in The High Temperature Superconducting Material $YBa_2Cu_3O_{7-x}$

Redacted for Privacy

Abstract approved : _____

John A. Gardner

The microstructure of the high temperature superconductor $YBa_2Cu_3O_{7-x}$ has been investigated by means of the perturbed angular correlation (PAC) spectroscopy technique. Sol gel prepared samples, doped with trace quantities of the radioactive isotope ^{111}In, show highly reproducible spectra. Data were taken between room temperature and 1070°C.

In the temperature regime below the orthorhombic to tetragonal phase transition temperature (23 - 600°C) the spectra are dominated by a site which shows a linear increase in the asymmetry parameter η and a linear decrease in the electric field gradient Vzz(lat) with increasing temperature.

This same site experiences the phase transition to the tetragonal structure at temperatures above 640°C, which is indicated by a jump in η and Vzz(lat) to lower values. The phase transition is reversible, showing that ^{111}In occupies a site in $YBa_2Cu_3O_{7-x}$.

Another site appears in the spectra when the temperature approaches the melting point of $YBa_2Cu_3O_{7-x}$. The increase of the fraction of this site is accompanied by the decrease of the fraction of the site mentioned above, but the sum of these two fractions remains constant.

Both sites disappear above the melting point of $YBa_2Cu_3O_{7-x}$. The former site is interpreted as ^{111}In substituted at the Yttrium lattice site, whereas the latter one is consistent with the hypothesis of ^{111}In

being substituted at a copper site whose population increases rapidly with temperature.

Perturbed Angular Correlation Spectroscopy in The High Temperature Superconducting Material $YBa_2Cu_3O_{7-x}$

by

Rainer Schwenker

A THESIS

submitted to

Oregon State University

in partial fulfillment of
the requirements for the
degree of

Master of Science

Completed December 3 , 1990

Commencement June 1991

Approved:

Redacted for Privacy

Professor of Physics in charge of major

Redacted for Privacy

Chairman of the Department of Physics

Redacted for Privacy

Dean of Graduate School

Date thesis is presented December 3, 1990

Typed by Rainer Schwenker for Rainer Schwenker

Table of Contents

Table of Contents

List of Figures

List of Figures

List of Tables

Perturbed Angular Correlation Spectroscopy in The High Temperature Superconducting Material $YBa_2Cu_3O_{7-x}$

1. Introduction

As soon as high-temperature superconductors were discovered, many specific measurement techniques were applied to find informations about these new materials. Macroscopic techniques like resistivity, specific heat and magnetic susceptibility measurements or microscopic techniques like perturbed angular correlation (PAC), muon spin rotation, Moessbauer spectroscopy, nuclear magnetic resonance and nuclear quadrupole resonance are some of them.

PAC spectroscopy, the technique used in this work, is a powerful tool since it can reveal information about the very local structure of the material under consideration. One necessary prerequisite is to know at which site in the crystal structure the probing atom is located. That turned out to be a problem when PAC was used to measure the ceramic oxide $YBa_2Cu_3O_{7-x}$. Not only is the site substitution ambigious, but it has proven difficult to dissolve the ^{111}In PAC probe into $YBa_2Cu_3O_{7-x}$ at all. The purpose of this work is to show that $YBa_2Cu_3O_{7-x}$ samples prepared by the sol gel method yield reproducible results and proper site identification.

1.1. The new copper-oxide based superconductors.

It was the discovery of the 35 K superconducting La-Ba-Cu-O system reported in April 1986 by J.G. Bednorz and K.A. Mueller [1], which started a research increase in the field of superconductivity. There have been innumerable investigations since then, to find other ceramic compounds with an even higher critical temperature. By replacing lanthanum of the La-Ba-Cu-O system with the smaller rare earth element yttrium, M.K.Wu, C.W. Chu and their co-workers [2], in February 1987, were able to produce the compound which is now known as $YBa_2Cu_3O_{7-x}$, or for short 1-2-3 , with a transition temperature of 92 K [3, 4] .

The materials of further investigations, being compositions of rare and alkaline earths, copper and oxygen, prove to be more complex. It is the compound $Tl_2Ba_2Ca_2Cu_3O_{10}$ which possesses the highest transition temperature of somewhat above 125 K at the present time [5,6] .

All of the new high-temperature superconductors have a common crystal lattice feature: they all contain planes of copper and oxygen atoms sandwiched between layers of the other elements. It is in these planes where the interactions responsible for superconductivity are believed to occur . The types of superconductivity (p-type conductivity due to holes, n-type conductivity due to electrons) can be correlated to the formal valence state of the copper atoms, neglecting the difference between the formal valence and the true charge, which arises from hybridization with oxygen 2p orbitals [7]. It is the change from copper's most stable valence state 2+ to 3+, called oxidation, or to 1+, called reduction, due to other oxidizing or reducing atoms, which delocalizes electrons and makes them available for electronic conduction. There also seems to be a critical fractional valence which is responsible for destroying antiferromagnetism and allowing superconductivity. For example, La_2CuO_4 has a copper valence of 2+ , but $La_{2-x}Ba_xCuO_4$

where barium is incorporated by solid solution, requires a higher valence value for copper. In the case of x=1, the valence would have been changed from 2+ to 3+. When the copper valence reaches a value of 2.2+, antiferromagnetism disappears and superconductivity appears.

As can be seen in figure 1.1, $YBa_2Cu_3O_7$ has a fully ordered crystal lattice consisting of unmixed (no solid solution) planes of yttrium (valence 3+) ions, barium (valence 2+)-oxide and copper (valence between 2+ and 3+)-oxide. In between the barium-oxide and yttrium layers, the copper (2) atoms are coordinated with oxygen in pyramids. The bases of these pyramids form the copper-oxygen plane necessary for superconductivity. Copper(1) atoms are coordinated with four oxygen atoms in a flat, diamond like shape. The corners are connected to form a chain of diamonds. Using the indicated valences (oxygen valence =2-) it can be seen that copper has an average valence of 2.33+ in $YBa_2Cu_3O_7$. As in $La_{1.8}Ba_{0.2}CuO_4$, again a copper valence value larger than 2+ is present, which is interpreted as the reason for positively charged holes in the conduction band and therefore p-type superconductivity. If $YBa_2Cu_3O_7$ is reduced in oxygen content to $YBa_2Cu_3O_6$ the material becomes insulating. Observations show that it is the connecting oxygen (1) between the copper (1) sites which is lost [10] (fig.1.2). In the $YBa_2Cu_3O_6$ crystal structure the copper (1) sites have a stable, chain-like copper-copper coordination with formal valence equal to 1+, whereas the copper (2) sites are not directly affected by the disappearance of the (1)oxygens, but change their formal valence to 2+.

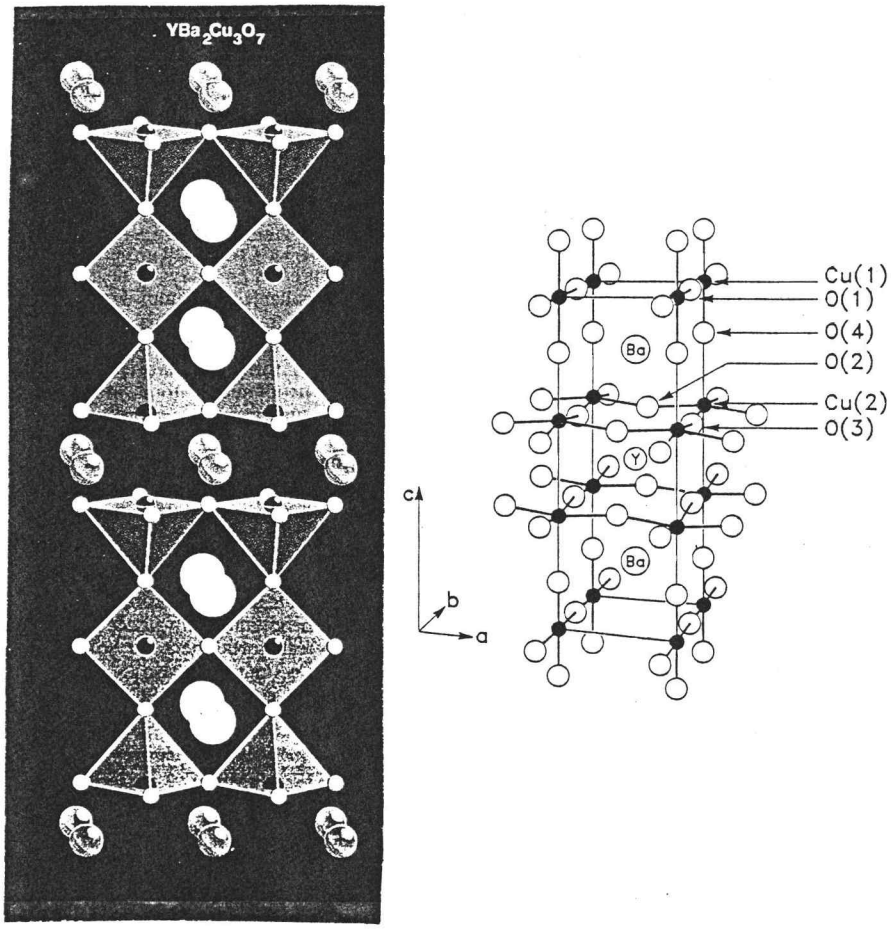

Fig. 1.1. Two perspectives on the crystal structure of YBa_2CuO_7 [8,9].

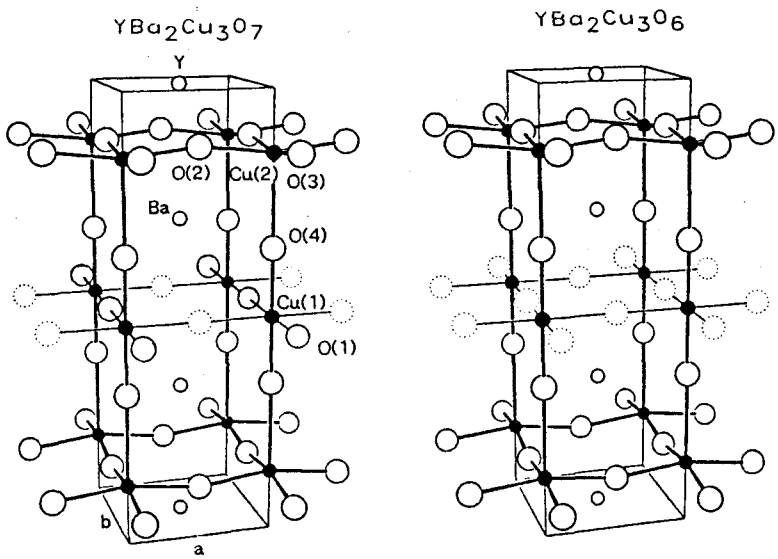

Fig. 1.2. Crystal structures of $YBa_2Cu_3O_7$ and $YBa_2Cu_3O_6$. Notice the missing O(1) in $YBa_2Cu_3O_6$ [11]. Dotted circles indicate oxygen vacancies.

For $YBa_2Cu_3O_6$ the electrons are localized by the effect of antiferromagnetism. This effect can be overcome if enough oxygen gets incorporated in the now "empty" copper-oxygen diamonds. At the level of 6.5 for example (meaning $YBa_2Cu_3O_{6.5}$), a compound with a distinct crystal structure is found [12], fig.1.3. . The chains of diamonds and sticks form an ordered array. $YBa_2Cu_3O_{6.5}$ has a transition temperature of 60 K.

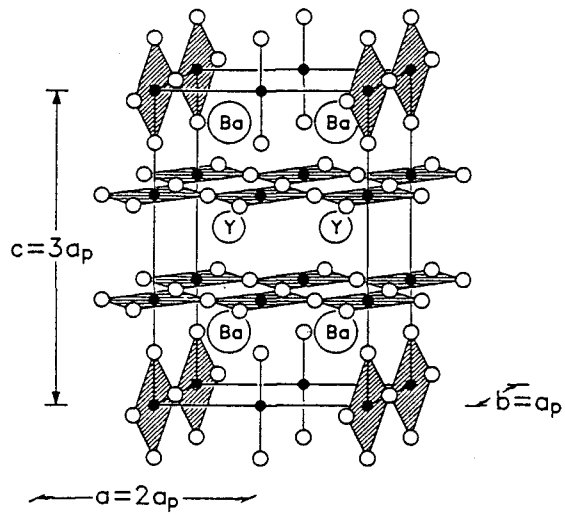

Fig. 1.3. Proposed real space structure for the $O_{6.5}$ phase [13].

An interesting comparison has been made by Cava et al. [7], showing that the formal valence of the plane copper versus the amount of (7-x) oxygens per unit cell, $0<x<1$, follows the same nonlinear behavior as does T_c versus x, see fig. 1.4. .

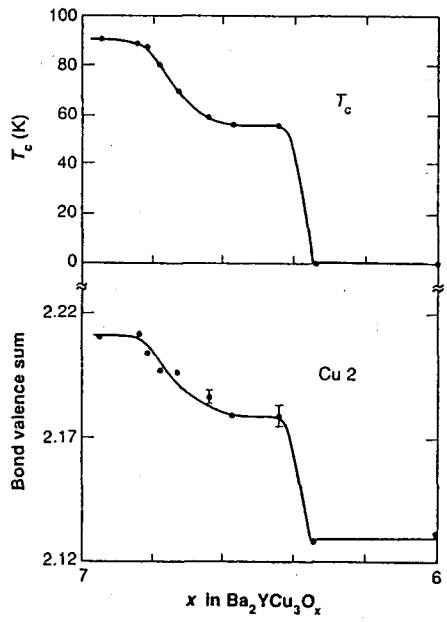

Fig. 1.4. **top**: Critical temperature Tc versus oxygen content in $YBa_2Cu_3O_x$. **bottom**: Valence of the plane copper for the same samples determined from neutron diffraction crystal analysis [7].

So far, the only n-type superconductor, a derivative of the Nd_2CuO_4 structure, was found in 1989 by Y.Tokura and coworkers [14]. As the comparison with the crystal structure of La_2CuO_4 shows (see fig.1.5) neodymium, which is smaller than lanthanum, has a different coordination of oxygen atoms, but a crystal structure which also involves copper oxygen planes. It is the replacement of Nd(valence3+) with atoms of similar size, but different valence value (4+), which produces n-type superconductivity. The compounds are $Nd_{2-x}Ce_xCuO_4$ and $Nd_{2-x}Th_xCuO_4$. The highest transition temperature is near 25 K (x=0.17). Calculating the formal valence of copper shows that its value decreased to 1.83, indicating the creation of carriers in the conduction band. These materials are not yet understood and remain a subject of intense research.

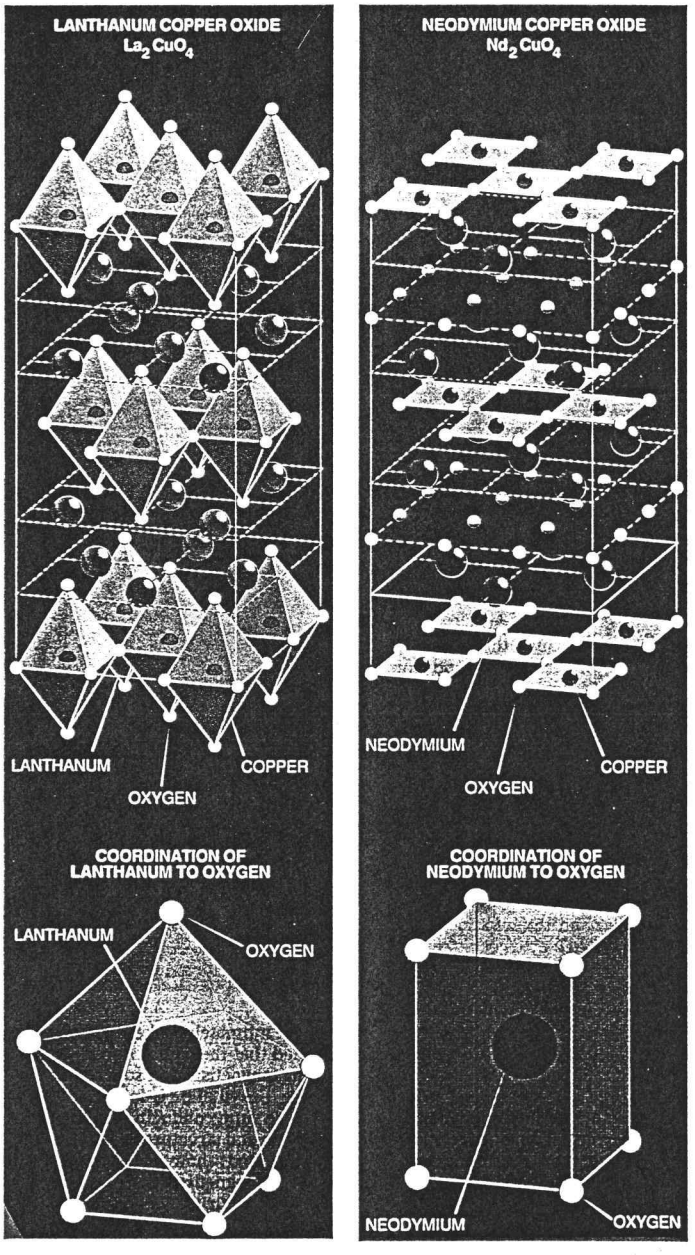

Fig. 1.5. Crystal structure of La_2CuO_4 and Nd_2CuO_4 [8].

1.2. The superconductor $YBa_2Cu_3O_{7-x}$

The superconductor $YBa_2Cu_3O_{7-x}$ is a member of the copper-oxide ceramic family $RBa_2Cu_3O_{7-x}$ (R = Y, Nd, Sm, Eu, Gd, Dy, Ho, Er, Tm, Yb, Ln). All of these high temperature superconductors exhibit a T_c around 90 K [15,16]. The superconducting properties of $YBa_2Cu_3O_{7-x}$ depend critically on the way the material is processed at higher temperatures. The atmospheric environment (air or oxygen for example), the annealing and cooling times, and the temperatures applied to the material control the oxygen content of the end-product. The ideal crystal structure of 123 at room-temperature, is an orthorhombic one, see fig. 1.2. . When the compound gets heated to higher temperatures, a change in the lattice constants can be observed, see fig. 1.6.

It has been found that a phase transition from orthorhombic to tetragonal occurs at a temperature around 600°C. The phase transition temperature decreases with decreasing oxygen pressure and is of special interest for PAC measurements, since the PAC probe is sensitive to structural changes. The data displayed in fig. 1.6 can be correlated with results found by an in-situ neutron diffraction experiment done by Jorgensen et al.[18]. They observe that the temperature dependent changes in the lattice parameters are caused by changes in oxygen content and order on the copper(1)-oxide plane, see fig. 1.7.

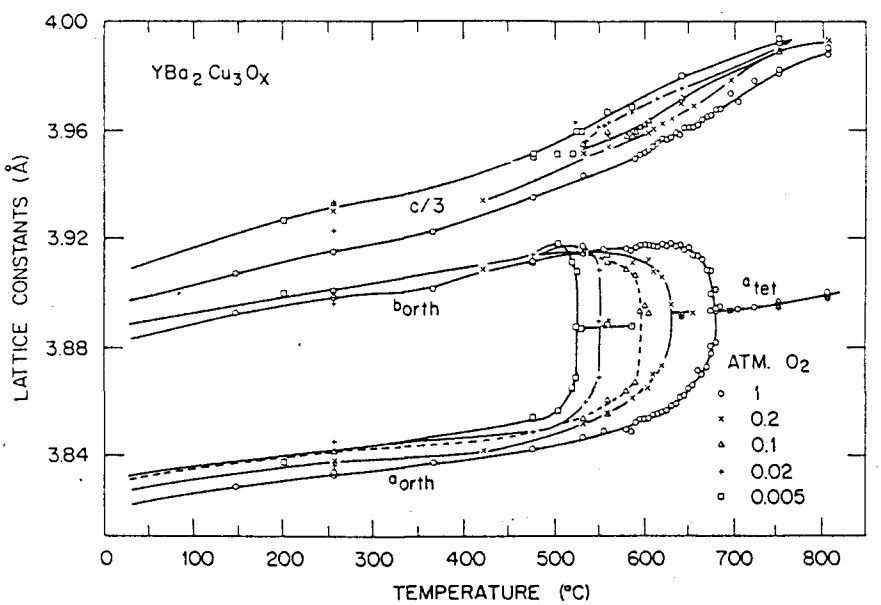

Fig. 1.6. Lattice constants versus temperature for various oxygen partial pressures. The orthorhombic-to-tetragonal transformation temperature decreases with decreasing oxygen pressure. The lines are to guide the eye [17].

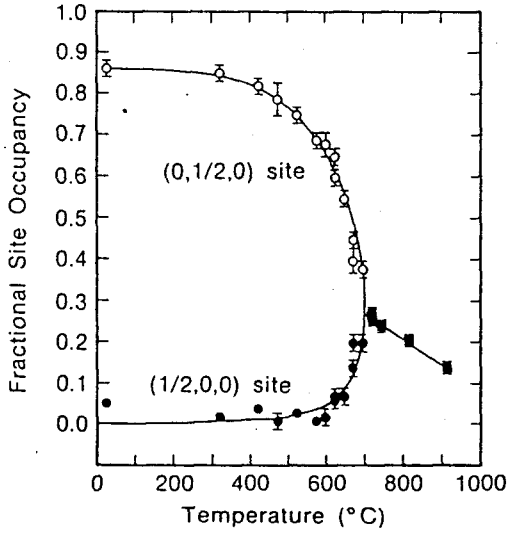

Fig. 1.7. Fractional oxygen site occupancies in the basal copper plane versus temperature for a sample heated in one atmosphere oxygen.

The removal of oxygen from its O(1) site has three effects on the 123 crystal structure:

* A negative thermal expansion of the b axis before the phase transition, due to loss of oxygen at the O(1) site [compare fig. 1.6, 1atm. O_2 and fig. 1.7, O(1)=(0,1/2,0) site].

* A positive thermal expansion of the a axis before the transition , due to an enhanced occupation of the normally vacant O(5) site [compare fig. 1.6, 1 atm.O_2 and fig. 1.7, O(5)=(1/2,0,0) site].

* When a- and b-axes obtain the same length and O(1) and O(5) sites show equal occupancy, the oxygen order-disorder phase transition occurs.

Oxygen continues to be withdrawn from the Cu(1)-oxygen plane at temperatures higher than the phase transition temperature . Fig. 1.8 shows in a comprehensive way how oxygen pressure, temperature, oxygen content of the sample and the location where the phase transition occurs, are related to each other.

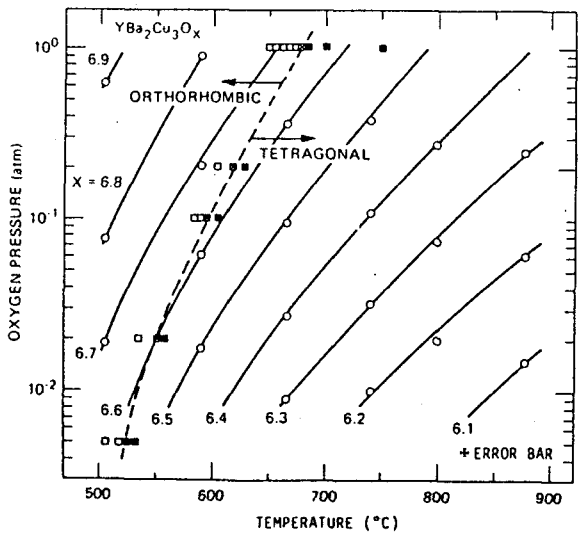

Fig. 1.8. Structural phase diagram for 123. Open squares indicate orthorhombic x-ray diffraction pattern, filled squares indicate tetragonal, and x-filled squares indicate the point of transformation. The oxygen content at the O-to-T transition and the transition temperature both decrease with decreasing oxygen partial pressure [19].

When a sample is prepared, it is normally cooled down slowly from 950°C to room temperature. At the tetragonal to orthorhombic transition temperature (around 670°C in air) an oxygen disorder - order phase transiton takes place. It is accompanied by the formation of twins. The boundaries of these twins build a {110} mirror plane, in which the a- and b-axes are interchanged across the boundary (see fig. 1.9).

C.J. Jou and J.Washburn propose in their model [21] a nucleation - and - growth mechanism for the twin formation. It has been concluded [22] that twin related domains originate at the grain boundaries to relax strain energy. So far there is a tendency to believe that the phase transition is a second - order transformation.

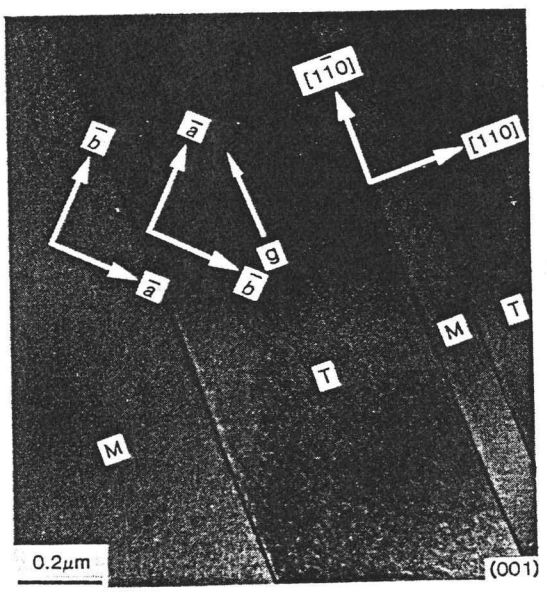

Fig. 1.9. Indexed matrix / twin structure for the Ba-Y-Cu-O superconducting material. The matrix and twin are seen to be rotated exactly by 90° to each other and the matrix / twin boundary,i.e., coherent twin boundary,lies on (100), which is seen edge-on [20].

1.2.1. Decomposition of $YBa_2Cu_3O_{7-x}$ and related phases

Commonly the superconductor $YBa_2Cu_3O_{7-x}$ is prepared by mixing appropriate quantities of Y_2O_3,BaO (or $BaCO_3$) and CuO together, pressing this mixture to form a pellet and calcining the pellet in an air or oxygen atmosphere for 12 hours between 900° and 950° C. X-ray diffraction patterns show that, in addition to 123, samples often contain tiny amounts of Y_2BaCuO_5 (for short 211) and $BaCuO_2$ (for short 011).

Roth et al. [23] investigated such samples in air in a temperature range from 950° up to 1050° C by conducting x-ray diffraction measurements on quenched samples. Between 950°- and 975° C the x-ray intensities for the materials other than to 123 and characteristic peaks associated with a quenched liquid, known from BaO - CuO system investigations, increase slightly. A more pronounced increase in intensity of these phases is found up to 1000° C. At 1005° C only the patterns belonging to 211, 011 and a quenched liquid are observed. In order for the ternary compound 123 to melt through a four-phase region, Roth et al. postulated an incorporation of atmospheric CO_2 into the reacting parts of the system. This conclusion found support from several other investigators concerned with the melting behavior of 123.

T.Aselage and K.Keefer [24] extended this work using differential thermal analysis, direct visual observations, x-ray diffraction and electron microprobe analysis. Their results were obtained in air at total pressure of 640 Torr (1Torr = 133 Pa). Their study of the binary join $BaCuO_2$ - CuO shows an eutectic between 912° and 920° C, which is a little higher than the 900° to 910°C reported by Roth et al.. The lowest melting point observed occured at 890° C for the eutectic between 123, CuO and 011. Table 1.1. summarizes published melting temperatures for 123, 211, 011 , $Y_2Cu_2O_5$ (=202) and CuO (=001) .

Table 1.1. Melting temperatures of 123, 211, 011, 202 and 002

Material	Temperature	atmosphere	group
123	1013	air	T.Aselage [24]
123	1002	air	R.Roth [23]
123	925	air	A.Ono [24,25]
123	993	air	J.Takada [24,26]
123	1020	air	F.Holzberg [24,27]
123	980 / 1020	air / oxygen	S.Takekava [24,28]
123	1015 / 1034	air / oxygen	K.Lay [29]
123	1015 / 1035	air / oxygen	P.Gallagher [29,30]
123	977 / 999	air / oxygen	N.Nevriva [29,31]
123	1004 / 1027	air / oxygen	F.Greuter [29,32]
123	999 / 1028	air / oxygen	R.McCallum [29,33]
011	950	air	K.Frase [34]
011	1007	air	R.Roth [23]
011	1010	air	T.Aselage [24]
211	1275	air	R.Roth [23]
211	1270	air	T.Aselage [24]
202	1122	air	T.Aselage [24]
202	1100-1150	air	R.Roth [23]
002	1026(decomp.)	air	T.Aselage [24]
002	1135(melt)	air	T.Aselage [24]

1.3. Perturbed angular correlation spectroscopy

The angular distribution of radiation from an atomic or nuclear system has a characteristic pattern with respect to a chosen axis. The study of the angular correlation of successive radiation from nuclei has been a very useful tool in nuclear physics. It provides a method for the determination of properties of the nuclear levels, of the radiation emitted, and of the interactions governing the emission [35]. Most of the angular correlation experiments are performed on nuclei embedded in condensed matter. Consequently the electric and magnetic fields originating from the surrounding matter are present at the nuclei. These perturbing fields interact with the electric and magnetic moments of the nuclei and often alter the angular correlation patterns of the successive radiations. Through analyzing the perturbed angular correlation (PAC) pattern, some physical quantities like strength and type of the interaction and crystal symmetry can be extracted with good accuracy, provided the necessary nuclear parameters are well-established. Among various types of angular correlations, gamma-gamma correlation is the most often employed one due to the penetrating power of gamma-rays in condensed matter. Gamma-gamma PAC spectroscopy has been used to study the defect -impurity association in metals [36-40], internal oxidation in metals [41,42], impurity effects in semiconductors [43,44], and phase identifications in compounds [45,46]. An extended list of TDPAC measurements on compounds has been compiled by Lerf and Butz [47], and a similar compilation for metals was done by Vianden [48].

1.3.1. ^{111}Cd as a PAC tracer nucleus

Radioactive ^{111}In, which has a half-life time of 2.83 days, decays through an electron-capture process to the excited state of its daughter

isotope ^{111}Cd, which subsequently decays to its ground state by emitting two cascade gamma-rays with energy 171 and 245 keV. After the electron-capture process, the electron hole in the K-shell of ^{111}Cd decays through x-ray emission and Auger processes. The Auger events result in a highly ionized probe atom. The recovery time of these exited ionic states will critically depend on the availability of free electrons in the surrounding environment of the probe atom. The recovery time is less than 10^{-12} sec for tracers embedded in metals, which is too short to give any detectable effect [49]. But in semiconductors and insulators, the electronic holes in the outermost shell could persist long enough to introduce an additional perturbation on the angular correlation pattern. The relevant nuclear characteristics of the electron-capture decay of ^{111}In to ^{111}Cd are summarized in table 1.2 and fig. 1.10 gives the decay scheme of the ^{111}In to ^{111}Cd transition.

Table 1.2. Summary [50] of relevant nuclear characteristics of ^{111}Cd

Parent half-life of ^{111}In	2.83 days
Energies of cascade gamma-rays:	
gamma 1	171.28(8) keV
gamma 2	245.42(7) keV
Nuclear-spin sequence:	7/2+ to 5/2+ to 3/2+
Angular-correlation coefficients:	
A2	- 0.180(2)
A4	≈0
Intermediate nuclear state:	
half-life	85.0(7) ns
electric quadrupole moment [51]	+ 0.83(13) b
magnetic dipole moment	- 0.7656(25)μ_N

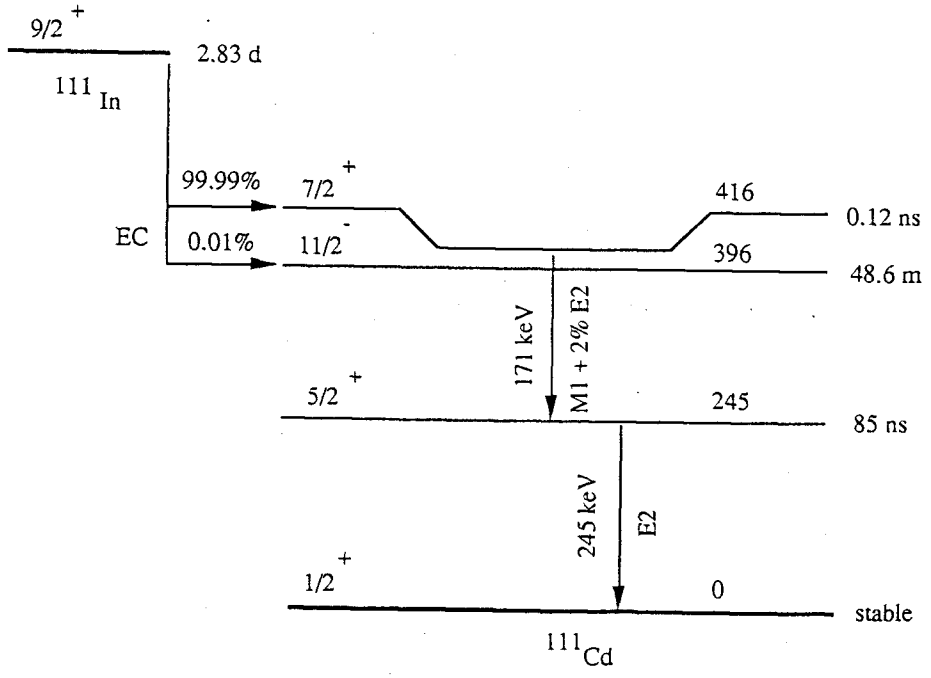

Fig. 1.10. The ^{111}In to ^{111}Cd decay in a schematic diagram [52].

2. Theory of gamma-gamma PAC

In this experiment 123 was investigated using a ^{111}In / ^{111}Cd PAC probe. The only important interaction between the PAC probe and the extranuclear field in this case is the one between the quadrupole moment of the probe and the electric field gradient (EFG) of the lattice. The reason for that is (i) higher order electric interactions are negligible, (ii) 123 is a non-magnetic material and therefore no magnetic interactions have to be taken into account, and (iii) the ^{111}In PAC probe has a closed electronic shell (spherical symmetry) and therefore no magnetic or electric dipole moments. The formalism for static EFG-quadrupole interaction that will be presented in this chapter follows closely that given by Frauenfelder and Steffen [49], as summarized by Jaeger [53], Su [54], and Fuchs [55]. A more modern treatment is given by Steffen and Adler [56] in a form that is more suitable for low temperature work. In this chapter the notation of Jaeger [53] and Su [54] was adopted.

2.1. The generalized angular correlation function $W(\mathbf{k}_1,\mathbf{k}_2,t)$

The probe nuclei of gamma-gamma PAC measurements decay through a cascade $I_i \rightarrow I \rightarrow I_f$, emitting two gamma-rays. The first gamma-ray is used to establish the quantization axis with respect to which the direction of the second gamma-ray is correlated. From the three existing nuclear states with spins I_i, I and I_f we find the sublevels of the intermediate state I populated with unequal probabilities during the decay. The **angular correlation function** $\mathbf{W(k_1,k_2,t)}$ is defined so that $W(\mathbf{k}_1,\mathbf{k}_2,t)d\Omega_1 d\Omega_2$ is the probability that gamma 1 and gamma 2 are emitted in directions $\mathbf{k}_1$ and $\mathbf{k}_2$ within the solid angles $d\Omega_1$ and $d\Omega_2$. The time "t" in $W(\mathbf{k}_1,\mathbf{k}_2,t)$ is the time separation between the two successive radiations, meaning t=0 is the time at which gamma 1 is emitted. The most general form of the PAC function, using the density matrix formalism, is

$$W(\mathbf{k}_1,\mathbf{k}_2,t) = \mathrm{Tr}\,[\rho(\mathbf{k}_1,t)\rho(\mathbf{k}_2,0)] \qquad (2\text{-}1)$$

where $\rho(\mathbf{k}_1,0)$ and $\rho(\mathbf{k}_2,0)$ are the density matrices which describe the system under discussion immediately after the emission of gamma 1 and gamma 2 respectively. In the presence of extra-nuclear perturbations the density matrix of the system after emission of gamma 1 will evolve in time. The density matrix right before the emission of gamma 2 can be expressed as:

$$\rho(\mathbf{k}_1,t) = \Lambda(t)\rho(\mathbf{k}_1,0)\Lambda(t)^{+} \qquad (2\text{-}2)$$

If the interaction Hamiltonian describing the extranuclear perturbation is K(t), then the time evolution operator of the system, $\Lambda(t)$, obeys the time dependent Schrödinger equation with $\Lambda(t=0)=1$.

If K doesn't depend on t during the lifetime of the intermediate state, Schrödinger's equation is solved by :

$$\Lambda(t) = \exp(-\tfrac{i}{\hbar}Kt) \qquad (2\text{-}3)$$

Let us call the sub-levels of the intermediate state $a, a', a'', .. b, b', \ldots$. These sublevels form a complete set of eigenstates of I^2 and I_z. Formula (2-1) can now be written in the following way :

$$W(\mathbf{k}_1,\mathbf{k}_2,t) = \sum_{aa'} <a|\rho(\mathbf{k}_1,t)|a'><a'|\rho(\mathbf{k}_2,0)|a> \qquad (2\text{-}4)$$

Using (2-2), the first matrix element in (2-4) can be rewritten as:

$$<a|\rho(\mathbf{k}_1,t)|a'> = \sum_{bb'} <b|\rho(\mathbf{k}_1,0)|b'><bb'|G(t)|aa'> \qquad (2\text{-}5)$$

where

$$< bb'|G(t)|aa'> \equiv < a|\Lambda(t)|b >< a'|\Lambda(t)|b' >^* \qquad (2\text{-}6)$$

In PAC measurements the polarization of the radiation is not observed. In that case we call $W(\mathbf{k}_1,\mathbf{k}_2,t)$ the **directional correlation function**. Using the Wigner-Eckart theorem, the matrix elements of $\rho(\mathbf{k}_1,0)$ and $\rho(\mathbf{k}_2,0)$ are calculated to be :

$$< b|\rho(\mathbf{k}_1,0)|b'> = \sum_{k_1 N_1} (-1)^{2I-I_i+b} A_{k_1}(1) \begin{pmatrix} I & I & k_1 \\ b' & -b & N_1 \end{pmatrix} \times \sqrt{4\pi}\, Y^*_{k_1 N_1}(\theta_1,\phi_1) \qquad (2\text{-}7)$$

$$< a'|\rho(\mathbf{k}_2,0)|a > = \sum_{k_2 N_2} (-1)^{k_2-I_f-a} A_{k_2}(2) \begin{pmatrix} I & I & k_2 \\ a' & -a & N_2 \end{pmatrix} \times \sqrt{4\pi}\, Y_{k_2 N_2}(\theta_2,\phi_2) \qquad (2\text{-}8)$$

here $A_{k1}(1) = A_{k1}(L_1 L_1' I_i I)$ and $A_{k2}(2) = A_{k2}(L_2 L_2' I_f I)$ are numbers which depend only on the spins of the nuclear states involved in the transition and the multipolarities of the emitted radiations. The overall normalization adopted here is $A_o = 1$. Inserting (2-5,7,8) into (2-4), $W(\mathbf{k}_1,\mathbf{k}_2,t)$ becomes:

$$W(\mathbf{k}_1,\mathbf{k}_2,t) = \sum_{k_1 k_2} \sum_{N_1 N_2} [(2k_1+1)(2k_2+1)]^{-\frac{1}{2}} A_{k_1}(1) A_{k_2}(2)\, G^{N_1 N_2}_{k_1 k_2}(t) \times Y^*_{k_1 N_1}(\theta_1,\phi_1)\, Y_{k_2 N_2}(\theta_2,\phi_2) \qquad (2\text{-}9)$$

$Y^{*}_{k_1N_1}(\theta_1,\phi_1)$ and $Y_{k_2N_2}(\theta_2,\phi_2)$ are the spherical harmonics and the constant factor 4π has been dropped since it plays no role in angular correlation calculations. The summation indices k_1 and k_2 are not related to the vectors $\mathbf{k}_1$ and $\mathbf{k}_2$. A very important part of (2-9) is the definition of the **perturbation factor** as:

$$G^{N_1N_2}_{k_1k_2}(t) = \sum_{aa'\,bb'} (-1)^{2I+a+b}[(2k_1+1)(2k_2+1)]^{\frac{1}{2}} \begin{pmatrix} I & I & k_1 \\ b' & -b & N_1 \end{pmatrix} \times \begin{pmatrix} I & I & k_2 \\ a' & -a & N_2 \end{pmatrix} < bb'|G(t)|aa'> \qquad (2\text{-}10)$$

Recalling (2-6) we see that it contains all the information about the interaction between the system and the extranuclear perturbations.

2.1.1. Angular correlation for free nuclei

If we consider the case that there are no extranuclear perturbations acting on the nuclei during the transition $I_i \rightarrow I \rightarrow I_f$, meaning K(t)=0 in (2-3), the time evolution operator $\Lambda(t)$ becomes unity and in (2-6) we end up with $< bb' \mid G(t) \mid aa' > = \delta_{a\,b}\,\delta_{a'\,b'}$. Applying this to (2-10) with the use of the orthogonality relation of 3–j symbols:

$$\sum_{aa'} \begin{pmatrix} I & I & k_1 \\ a' & -a & N_1 \end{pmatrix} \begin{pmatrix} I & I & k_2 \\ a' & -a & N_2 \end{pmatrix} = (2k+1)^{-1}\,\delta_{k_1k_2}\delta_{N_1N_2} \qquad (2\text{-}11)$$

the perturbation factor becomes

$$G^{N_1N_2}_{k_1k_2}(t) = \delta_{k_1k_2}\delta_{N_1N_2} \qquad (2\text{-}12)$$

This result inserted in (2-9) yields to the unperturbed, time independent form of the perturbed angular correlation function :

$$W(\mathbf{k}_1, \mathbf{k}_2) = \sum_{k=0,\text{even}}^{k_{max}} A_k(1)\, A_k(2)\, P_k(\cos\theta) = \sum_{k=0,\text{even}}^{k_{max}} A_{k\,k} P_k(\cos\theta)$$

(2-13)

where $P_k(\cos\theta)$ are the Legendre polynomials and θ is the angle between the two cascade radiations.

The selection rule for 3-J symbols restricts the value of k between 0 and 2I. In this case we have I=5/2 and therefore find k_{max} = 4. Since the circular polarization of the emitted radiation is not observed, only even values of k have to be taken into account. It should be mentioned that A_4 is much smaller than A_2.

2.1.2. Static perturbation of a single nucleus

If we have a static extranuclear perturbation, meaning the field environment at the nucleus is constant in direction and in magnitude, than K(t)=K and the time evolution operator, as shown in (2-3), becomes :

$$\Lambda(t) = \exp(-\tfrac{i}{\hbar} K t) \qquad (2\text{-}14)$$

Let U be the unitary operator that diagonalizes the time–independent interaction Hamiltonian K :

$$U K U^{-1} = E \qquad (2\text{-}15)$$

Transformed in that way , E represents the diagonal energy matrix with energy eigenvalues E_n on the diagonal. The mathematical properties of the exponential function allows us to transform (2-14) into :

$$U^{-1} e^{-\frac{1}{\hbar} K t} U = e^{-\frac{1}{\hbar} E t} \qquad (2\text{-}16)$$

Now the matrix elements of $\Lambda(t)$, necessary to know in (2-6), become :

$$< a|\Lambda(t)|b >= \sum_{n} < n|b > * < n|a > \exp(-\tfrac{1}{\hbar} E_n t) \qquad (2\text{-}17)$$

The vectors indicated by n are the eigenstates of the diagonalized Hamiltonian, describing the n^{th} level of the intermediate state.

The following notation for the argument in the exponential will be used :

$$\exp(-int) \equiv \exp(-\tfrac{i}{\hbar} E_n t) \qquad (2\text{-}18)$$

The perturbation function in (2-10) can now be written as:

$$G_{k_1 k_2}^{N_1 N_2}(t) = \sum_{\substack{aa' \\ bb'}} \sum_{nn'} (-1)^{2I+a+b} [(2k_1+1)(2k_2+1)]^{\frac{1}{2}} \begin{pmatrix} I & I & k_1 \\ a' & -a & N_1 \end{pmatrix}$$

$$\times \begin{pmatrix} I & I & k_2 \\ b' & -b & N_2 \end{pmatrix} \exp[-i(n-n')t] < n|b > * < n|a >< n'|b' >< n'|a' > * \qquad (2\text{-}19)$$

This formula is also valid for static interaction in a single crystal.

2.1.3 Static perturbations in polycrystalline material

In this work the angular correlation experiments were carried out with ^{111}In nuclei in polycrystalline samples. It is assumed that the polycrystalline sample consists of a large number of randomly oriented microcrystals. Let $D(\Omega)$ be the rotation matrix that transforms the

interaction Hamiltonian $K(\mathbf{z})$ from the lab coordinate frame $\mathbf{z}$ through a set of prescribed Euler angles $\Omega = (\phi, \theta, \gamma)$ to the principal axes system $\mathbf{z}'$ of a microcrystal:

$$K(\mathbf{z}') = D(\Omega)\, K(\mathbf{z})\, D^{-1}(\Omega) \tag{2-20}$$

Similar to (2-15) the unitary operator U diagonalizes $K(\mathbf{z}')$

$$U\, K(\mathbf{z}')\, U^{-1} = E \tag{2-21}$$

and the time evolution operator is transformed by :

$$\Lambda(t) = D^{-1}(\Omega)\, U^{-1} \exp(-\tfrac{i}{\hbar} Et)\, U\, D(\Omega) \tag{2-22}$$

with (2-22) the matrix elements of $\Lambda(t)$ can be rewritten as:

$$< a|\Lambda(t)|b >= \sum_{m_1 m_2 n} < n|m_1 >^* < n|m_2 > \exp(-int) D^{I}_{m_1 a}{}^{*}(\Omega) D^{I}_{m_2 b}(\Omega)$$

(2-23)

where terms of type $D^{I}_{m\ a} = <m \mid D(\Omega) \mid a>$ are the matrix elements for the rotation operator. Using (2-23), equation (2-6) obtains the following form :

$$< bb'|G(t)|aa'>= \sum_{\substack{m_1 m_2 \\ m_1' m_2'}} \sum_{nn'} < n|m_1 >^* < n'|m_1' >< n|m_2 >< n'|m_2' >^*$$

$$\times \exp[-i(n-n')] D^{I}_{m_1 a}{}^{*}(\Omega) D^{I}_{m_1' a'}(\Omega) D^{I}_{m_2 a}(\Omega) D^{I}_{m_2' b'}{}^{*}(\Omega)$$

(2-24)

The contraction relation for the rotation matrix elements [57]

$$\begin{pmatrix} j_1 & j_2 & j \\ m_1' & m_2' & m' \end{pmatrix} D^{j}_{mm'}{}^{*} = \sum_{m_1 m_2} \begin{pmatrix} j_1 & j_2 & j \\ m_1 & m_2 & m \end{pmatrix} D^{j_1}_{m_1 m_1'} D^{j_2}_{m_2 m_2'} \tag{2-25}$$

can be used to reduce equation (2-24).
The perturbation factor in (2-10),

$$G^{N_1 N_2}_{k_1 k_2}(t) = \sum_{a a' b b'} (-1)^{2I+a+b} [(2k_1+1)(2k_2+1)]^{\frac{1}{2}} \begin{pmatrix} I & I & k_1 \\ b' & -b & N_1 \end{pmatrix} \times \begin{pmatrix} I & I & k_2 \\ a' & -a & N_2 \end{pmatrix} < bb'|G(t)|aa'> \tag{2-10}$$

after summing over all sublevels a, a', b, b', becomes :

$$G^{N_1 N_2}_{k_1 k_2}(t) = \sum_{\substack{m_1 m_2 \\ m_1' m_2'}} \sum_{nn'} (-1)^{2I+m_1+m_2} [(2k_1+1)(2k_2+1)]^{\frac{1}{2}} \exp[-i(n-n')t] \times \begin{pmatrix} I & I & k_1 \\ m_1' & -m_1 & p_1 \end{pmatrix} \begin{pmatrix} I & I & k_2 \\ m_2' & -m_2 & p_2 \end{pmatrix} D^{k_1}_{p_1 N_1}{}^{*}(\Omega) D^{k_2}_{p_2 N_2}(\Omega) \times < n|m_1>^{*} < n'|m_1'>< n|m_2>< n'|m_2'>^{*} \tag{2-26}$$

Due to the fact, that each one of the microcrystals resembles a different rotationmatrix, the perturbation factor for a randomly oriented polycrystalline sample is obtained by averaging (2-26) over all the possible orientations of its constituent microcrystals. The orthogonality relation for the rotation matrix is

$$\int d\Omega \, D^{j_1}_{m_1 m_1}{}^{*}(\Omega) \, D^{j_2}_{m_2 m_2}(\Omega) = \frac{1}{2j_1+1} \delta_{j_1 j_2} \delta_{m_1 m_2} \delta_{m_1' m_2'} \tag{2-27}$$

Formula (2-27) allows us to obtain from (2-26) the "averaged" perturbation factor

$$G_{k\,k}(t) = \delta_{k_1 k_2}\,\delta_{N_1 N_2}\,\delta_{p_1 p_2} \sum_{n\,n'} S_{n\,n'}^{k_1 k_2} \exp[-i(n-n')t] \qquad (2\text{-}28)$$

with coefficients $S_{nn',k1k2}$ being defined as:

$$S_{n\,n'}^{k_1 k_2} = \sum_{\substack{m_1 m_2 \\ m_1' m_2'}} (-1)^{2I+m_1+m_2} \begin{pmatrix} I & I & k_1 \\ m_1' & -m_1 & p \end{pmatrix} \begin{pmatrix} I & I & k_2 \\ m_2' & -m_2 & p \end{pmatrix}$$

$$\times < n|m_1 >^* < n'|m_1' >< n|m_2 >< n'|m_2' >^* \qquad (2\text{-}29)$$

The perturbation factor for a polycrystalline sample becomes :

$$G_{k\,k}(t) = \sum_{\substack{m_1 m_2 \\ m_1' m_2'}} \sum_{n\,n'} (-1)^{2I+m_1+m_2} \begin{pmatrix} I & I & k \\ m_1' & -m_1 & p \end{pmatrix} \begin{pmatrix} I & I & k \\ m_2' & -m_2 & p \end{pmatrix}$$

$$\times \exp[-i(n-n')t] < n|m_1 >^* < n'|m_1' >< n|m_2 >< n'|m_2' >^* \qquad (2\text{-}30)$$

Comparing (2-30) with the single crystal result in (2-19),

$$G_{k_1 k_2}^{N_1 N_2}(t) = \sum_{\substack{aa' \\ bb'}} \sum_{n\,n'} (-1)^{2I+a+b} [(2k_1+1)(2k_2+1)]^{\frac{1}{2}} \begin{pmatrix} I & I & k_1 \\ a' & -a & N_1 \end{pmatrix}$$

$$\times \begin{pmatrix} I & I & k_2 \\ b' & -b & N_2 \end{pmatrix} \exp[-i(n-n')t] < n|b >^* < n|a >< n'|b' >< n'|a' >^* \qquad (2\text{-}19)$$

the perturbation function for the polycrystalline sample can be understood as the average of the perturbation function of the single crystal, written as

$$G_{kk}(t) = \frac{1}{2k+1} \sum_{p} G_{kk}^{pp}(t) \qquad (2\text{-}31)$$

For that reason the perturbation function for a polycrystalline sample is also called the **attenuation factor**. The sum in (2-28) can be decoupled by writing :

$$G_{kk}(t) = \sum_{n} S_{nn}^{kk} + \sum_{n \neq n'} S_{nn'}^{kk} \cos\left[\frac{(E_n - E_{n'})t}{\hbar}\right] \qquad (2\text{-}32)$$

Inserting (2-32) in the expression for the directional angular correlation function (2-9), the summation over N_1, N_2 can be performed since the perturbation function is independent of N_1 and N_2. The addition theorem for the spherical harmonics can also be applied to (2-9) and we end up with the very important result for the **directional correlation function displayed by a polycrystalline sample with static interactions**

$$W(\theta,t) = \sum_{k=0,\text{even}}^{k_{max}} A_{kk}\, G_{kk}(t)\, P_k(\cos\theta) \qquad (2\text{-}33)$$

An important feature of the perturbation function (2-32) for the polycrystalline sample is the time independent term $\sum_{n} S_{nn}^{kk}$. Because of this constant term, the angular correlation of a polycrystalline sample is never completely destroyed under the influence of static perturbing fields. For this reason, this term has historically been called the "**hard-core**".

2.2. The static electric quadrupole interaction

To be able to apply equation (2-32) it is necessary to find the energies En and En'. As said before, only the interaction between the quadrupole moment of the probe and the electric field gradient of its surrounding has to be considered. The **Hamiltonian for static electric interactions** of a nucleus with its environment is

$$H_{EI} = \sum_{ij} \frac{e_i e_j}{|\mathbf{r}_i - \mathbf{r}_j|} \tag{2-34}$$

where the quantities with index "i" are the charges and coordinates of the nucleus and the quantities with index j are those of its environment. Since the assumption of surrounding point charges calls for $r_j > r_i$, equation (2-34) can be expanded to become :

$$H_{EI} = \sum_{ij} \sum_{k=0}^{\infty} \frac{e_i e_j r_i^k}{r_j^{k+1}} P_k(\cos\theta_{ij}) \tag{2-35}$$

Here θ_{ij} is the angle between a pair of $\mathbf{r}_i$ and $\mathbf{r}_j$. Applying the addition theorem of spherical harmonics to (2-35) yields

$$H_{EI} = 4\pi \sum_{k=0}^{\infty} \frac{1}{2k+1} \sum_{\mu} (-1)^{\mu} \sum_{i} e_i r_i^k Y_{k\mu}(\theta_i,\phi_i) \sum_{j} e_j \frac{1}{r_j^{k+1}} Y_{k-\mu}(\theta_j,\phi_j) \tag{2-36}$$

The introduction of the tensor operator of the nuclear moments, $q^{(k)}$

$$q_{\mu}^{(k)} = \sum_{i} e_i r_i^k Y_{k\mu}(\theta_i,\phi_i) \tag{2-37}$$

the tensor operator for the fields, $V^{(k)}$ [58]

$$V_{\mu}^{(k)} = \sum_{j} e_j \frac{1}{r_j^{k+1}} Y_{k-\mu}(\theta_j, \phi_j) \tag{2-38}$$

and the scalar product of two tensor operators

$$q^{(k)} \bullet V^{(k)} = \sum_{\mu=-k}^{k} (-1)^{\mu} q_{\mu}^{(k)} V_{-\mu}^{(k)} \tag{2-39}$$

a more compact form of equation (2-36) can be achieved

$$H_{EI} = \sum_{k=0}^{\infty} \frac{4\pi}{2k+1} q_{\mu}^{(k)} \bullet V_{-\mu}^{(k)} \tag{2-40}$$

In equation (2-40) the Hamiltonian appears to be a product of two factors, a nuclear moment factor and an external field factor . In (2-41) the typically interacting terms of the sum in (2-40) : the charge with the external potential, the dipole with the electric field, the quadrupole with the field gradient, and so on are shown.

$$H_{EI} = 4\pi[Ze_i V^{(0)} + \frac{1}{3} \sum_{\mu=-1}^{1} (-1)^{\mu} q_{\mu}^{(1)} V_{-\mu}^{(1)} + \frac{1}{5} \sum_{\mu=-2}^{2} (-1)^{\mu} q_{\mu}^{(2)} V_{-\mu}^{(2)}$$

$$+ \frac{1}{7} \sum_{\mu=-3}^{3} (-1)^{\mu} q_{\mu}^{(3)} V_{-\mu}^{(3)} + \ldots] \tag{2-41}$$

But not every term has to be taken into account. The odd order electric moments vanish due to the requirement of parity conservation under reflection and the effects of nuclear electric hexadecapole moments or higher order terms are negligible. The only term that

remains in the electric interaction is the quadrupole term and its corresponding interaction Hamiltonian H_{QI} :

$$H_{QI} = \frac{4}{5}\pi\, T^{(2)} \bullet q^{(2)} = \frac{4}{5}\pi \sum_{\mu=-2}^{2} (-1)^{\mu}\, q_{\mu}^{(2)}\, V_{-\mu}^{(2)} \qquad (2\text{-}42)$$

$V^{(2)}$ is often called the classical electric field gradient (EFG) operator and $q^{(2)}$ is the second–rank tensor operator of the nuclear quadrupole moment.

The five components of $V_{\mu}^{(2)}$ can be written in terms of the Cartesian derivatives V_{xx}, V_{xy}, etc.,

$$V_0^{(2)} = \sqrt{\frac{5}{16\pi}}\, V_{zz} \qquad (2\text{-}43)$$

$$V_{\pm 1}^{(2)} = \mp \sqrt{\frac{5}{24\pi}}\, (V_{xz} - i V_{yz}) \qquad (2\text{-}44)$$

$$V_{\pm 2}^{(2)} = \sqrt{\frac{5}{96\pi}}\, (V_{xx} - V_{yy} - i 2 V_{xy}) \qquad (2\text{-}45)$$

If the principal axes system is chosen as the coordinate system, the cross derivatives in (2-44) and (2-45) disappear. With the definition of the **asymmetry parameter** η :

$$\eta = \frac{V_{xx} - V_{yy}}{V_{zz}} \qquad (2\text{-}46)$$

the principal axes components of $V_{\mu}^{(2)}$ become

$$V_0^{(2)} = \sqrt{\frac{5}{16\pi}}\, V_{zz} \qquad (2\text{-}47)$$

$$V_{\pm 1}^{(2)} = 0 \qquad (2\text{-}48)$$

$$V_{\pm 2}^{(2)} = \sqrt{\frac{5}{96\pi}}\,(V_{xx} - V_{yy}) = \sqrt{\frac{5}{96\pi}}\;\eta\, V_{zz} \qquad (2\text{-}49)$$

The system is called axially symmetric if $V_{xx}=V_{yy}$.

Conventionally, the principal system is chosen such that $|V_{xx}| \le |V_{yy}| \le |V_{zz}|$. This restricts η to $0 \le \eta \le 1$. At the nucleus Poisson's equation reduces to Laplace's equation and $V_{xx} + V_{yy} + V_{zz} = 0$. Thus **the EFG tensor is sufficiently characterized by the magnitude of the largest component V_{zz} and asymmetry parameter** η. The matrix elements of the quadrupole Hamiltonian (2-42) are

$$\langle Im|H_{QI}|Im'\rangle = \frac{4\pi}{5} \sum_{\mu=-2}^{2} (-1)^{\mu} \langle Im|q_{\mu}^{(2)}|Im'\rangle\, V_{-\mu}^{(2)} \qquad (2\text{-}50)$$

Note that the electric field gradient components don't appear as operators. The matrix elements of the quadrupole moment tensor can be evaluated using the Wigner–Eckart theorem [57] :

$$\langle Im|q_{\mu}^{(2)}|Im'\rangle = (-1)^{I-m} \begin{pmatrix} I & I & 2 \\ m' & -m & \mu \end{pmatrix} \langle I||q^{(2)}||I\rangle \qquad (2\text{-}51)$$

It is easy to see that $\langle I||q^{(2)}||I\rangle$, called the reduced matrix element, can be calculated using the conventional definition of the nuclear quadrupole moment [59] :

$$eQ = \sqrt{\frac{16\pi}{5}} < II|q_0^{(2)}|II> \qquad (2-52)$$

and letting m = I in (2–51) :

$$< I||q^{(2)}||I >= \sqrt{\frac{16\pi}{5}} \begin{pmatrix} I & I & 2 \\ I & -I & 0 \end{pmatrix}^{-1} eQ \qquad (2-53)$$

With this new definition, the matrix elements of the quadrupole moment tensor do have the form :

$$< Im|q_\mu^{(2)}|Im'>= (-1)^{I-m} \sqrt{\frac{5}{16\pi}} eQ \begin{pmatrix} I & I & 2 \\ m' & -m & \mu \end{pmatrix} \begin{pmatrix} I & I & 2 \\ I & I & 0 \end{pmatrix}^{-1} \qquad (2-54)$$

In the principal axes system, only the diagonal and two–off diagonal terms of the quadrupole Hamiltonian matrix (2–50) are not equal to zero. Expressing the EFG components in Cartesian derivatives (2.47-2.49) and defining the quadrupole frequency ω_Q as

$$\omega_Q = \frac{e\,Q\,V_{zz}}{4I(2I-1)\hbar} \qquad (2\text{-}55)$$

the non–vanishing matrix elements of the quadrupole Hamiltonian become :

$$< Im-2|H_{QI}|Im >= \hbar\omega_Q \frac{\eta}{2} [(I \pm m + 1)(I \pm m + 1)(I \mp m + 1)(I \mp m)]^{\frac{1}{2}} \qquad (2\text{-}56)$$

$$< Im|H_{QI}|Im >= \hbar\omega_Q [3m^2 - I(I+1)] \qquad (2\text{-}57)$$

2.2.1. Static electric quadrupole interaction in the case of axially symmetry ($\eta = 0$)

For the axially symmetric case $\eta = 0$, the off diagonal elements of the quadrupole Hamiltonian are equal to zero. The remaining energy eigenvalues are the diagonal elements of (2-57) :

$$E_m = \hbar\omega_Q [3m^2 - I(I+1)] \qquad (2\text{–}58)$$

There are (2 I + 1)/2 (for half–integer I) or I +1 (for integer I) distinct energy values since the ± m levels are doubly degenerate. The perturbation function (2-32) for a polycrystalline sample with axially symmetric electric quadrupole interaction

$$G_{k\,k}(t) = \sum_{n} S^{k\,k}_{n\,n} + \sum_{n \neq n'} S^{k\,k}_{n\,n'} \cos\left[\frac{(E_n - E_{n'})t}{\hbar}\right] \qquad (2\text{-}32)$$

now becomes :

$$G_{k\,k}(t) = \sum_{m} S^{k\,k}_{m\,m} + \sum_{m \neq > m'} S^{k\,k}_{m\,m'} \cos[3\omega_Q (m^2 - m'^2)t] \qquad (2\text{–}59)$$

Introducing a new index n = | m^2 – m' ^{2} |/2 (for half–integer I) or n = | m^2 – m' ^{2} | (for integer I) and defining

$$S_{k\,n} = \sum_{m\,m'} S^{k\,k}_{m\,m'} = \sum_{m\,m'} \begin{pmatrix} I & I & k \\ m' & -m & p \end{pmatrix}^2 \qquad (2\text{–}60)$$

the angular correlation function in (2–59) becomes

$$G_{kk}(t) = S_{k0} + \sum_{n>0} S_{kn} \cos(n\omega_0 t) \qquad (2\text{–}61)$$

The angular frequency ω_0, equivalent to the smallest non–vanishing energy difference, is equal to $6\omega_Q$ (for half–integer I) or $3\omega_Q$ (for integer I). The S_{kn} are normalized to $\sum_n S_{kn} = 1$.

2.2.2. .Static electric quadrupole interaction in the case of non-axially symmetry applied to intermediate states with I = 5 /2

If the interaction Hamiltonian (2-56,2-57) is not axially symmetric, it has to be diagonalized to find the energy eigenvalues. If I = 5/2, as it is for the nuclear spin of the intermediate state of ^{111}Cd, the Hamiltonian matrix looks like:

$$H_{QI} = \hbar\omega_Q \begin{pmatrix} 10 & 0 & \eta\sqrt{10} & 0 & 0 & 0 \\ 0 & -2 & 0 & 3\eta\sqrt{2} & 0 & 0 \\ \eta\sqrt{10} & 0 & -8 & 0 & 3\eta\sqrt{2} & 0 \\ 0 & 3\eta\sqrt{2} & 0 & -8 & 0 & \eta\sqrt{10} \\ 0 & 0 & 3\eta\sqrt{2} & 0 & -2 & 0 \\ 0 & 0 & 0 & \eta\sqrt{10} & 0 & 10 \end{pmatrix} \qquad (2\text{–}62)$$

The analytical solution to the secular equation can be found in the literature [60] and is described as:

$$E_1 = u + v \qquad (2\text{–}63)$$

$$E_{2,3} = -\frac{[(u+v) \mp i\sqrt{3}\,(u-v)]}{2} \qquad (2\text{–}64)$$

$$u, v = \hbar\omega_Q \alpha \sqrt[3]{\beta^2 - \sqrt{(\beta^2 - 1)}} \qquad (2\text{–}65)$$

where

$$\alpha = \sqrt{\frac{28}{3}(\eta^2 + 3)} \qquad \text{and} \qquad \beta = \frac{80\,(1-\eta^2)}{\alpha^3} \tag{2-66}$$

The energy eigenvalues, as functions of Vzz and η have the form :

$$E_{\pm\frac{5}{2}} = 2\alpha\hbar\omega_Q \cos[\tfrac{1}{3}\cos^{-1}\beta] \tag{2-67}$$

$$E_{\pm\frac{3}{2}} = -2\alpha\hbar\omega_Q \cos[\tfrac{1}{3}(\pi + \cos^{-1}\beta)] \tag{2-68}$$

$$E_{\pm\frac{1}{2}} = -2\alpha\hbar\omega_Q \cos[\tfrac{1}{3}(\pi - \cos^{-1}\beta)] \tag{2-69}$$

As before, we introduce the index n = | m^2 – m' ^{2} |/2, and the expression of the **perturbation factor for polycrystalline samples** (2-32) becomes :

$$G_{k\,k}(t) = S_{k\,0} + \sum_{n=1}^{3} S_{k\,n} \cos[\,\omega_n(\eta)\,t\,] \tag{2-70}$$

The so called **PAC frequencies** ω_n are defined as the differences between the energy eigenvalues of (2-67), (2-68) and (2-69) :

$$\omega_1 = |E_{3/2} - E_{1/2}| = 2\sqrt{3}\,\alpha\omega_Q \sin[\tfrac{1}{3}\cos^{-1}\beta\,] \tag{2-71}$$

$$\omega_2 = |E_{5/2} - E_{3/2}| = 2\sqrt{3}\,\alpha\omega_Q \sin[\tfrac{1}{3}(\pi - \cos^{-1}\beta)] \tag{2-72}$$

$$\omega_3 = |E_{5/2} - E_{1/2}| = 2\sqrt{3}\,\alpha\omega_Q \sin[\tfrac{1}{3}(\pi + \cos^{-1}\beta)] \tag{2-73}$$

with the important **sum rule** $\omega_3 = \omega_1 + \omega_2$. Fig. 2.1 shows how the eigenvalues of H_{QI} and the PAC frequencies depend on η.

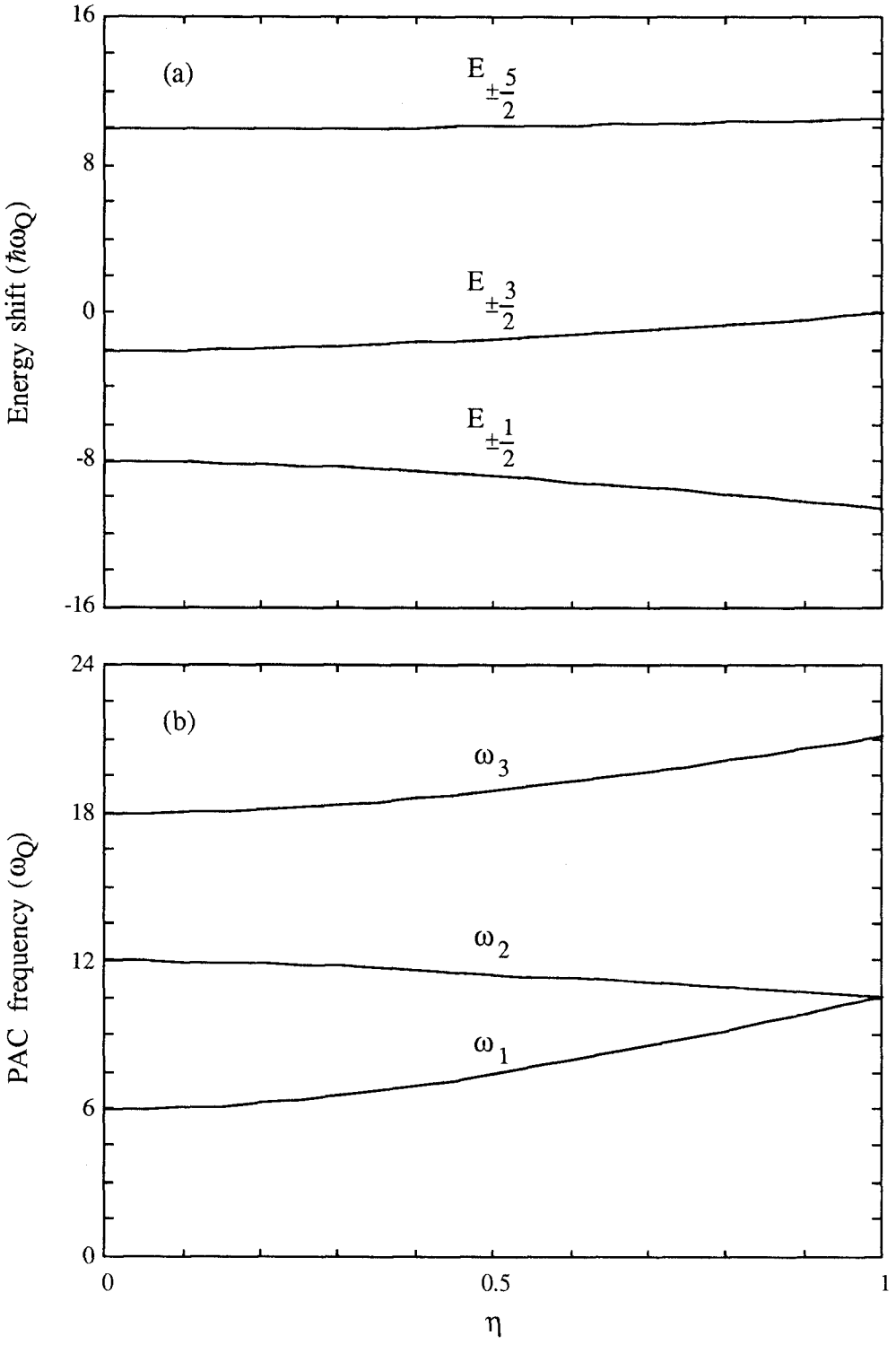

Fig. 2.1. (a) Eigenvalues and (b) PAC frequencies of the H_{QI} as functions of η for I = 5/2. The eigenstates are doubly degenerate.

The S_{kn} coefficients in (2-72), as known functions of the asymmetry parameter η [61], are displayed in table 2.1.

An approximate expression for the directional correlation function (since $A_4 < 1\% A_2$) can now be written as :

$$W(\theta,t) \approx 1 + A_2 G_2(t) P_2(\cos\theta) \qquad (2\text{-}74)$$

An important result since it is used (as will be shown later) to deduce $G_{22}(t)$ from measuring (2-74). The theoretical perturbation function $G_{22}(t)$, for various values of asymmetry parameter η is shown in Fig. 2.2.

2.2.3. Line broadening due to an EFG distribution

So far we have assumed all the microcrystals contained in a polycrystalline sample are perfect. But in a real crystal there always exist imperfections such as impurities and lattice defects. Two types of distribution models, Gaussian and Lorentzian distributions, are most often used to account for the small variations in the electric field gradient due to these imperfections. The distribution of the EFG magnitude is often assumed to be characterized by a **relative width** $\delta = \Delta V_{zz}/V_{zz}$.

If $P(\omega - \omega_0)$ describes one of the two normalized distribution functions, then the measured perturbation function is the convolution of the theoretical perturbation function (2-70) and the distribution function:

Table 2.1. Skn coefficients (k = 2, 4) for a general static H_{QI} as a function of η with I = 5/2.

η	S_{20} S_{40}	S_{21} S_{41}	S_{22} S_{42}	S_{23} S_{43}
0.0	0.2000 0.1111	0.3714 0.2381	0.2857 0.2857	0.1429 0.3651
0.1	0.2024 0.1098	0.3688 0.2395	0.2855 0.2858	0.1432 0.3649
0.2	0.2090 0.1061	0.3617 0.2435	0.2850 0.2861	0.1443 0.3643
0.3	0.2181 0.1010	0.3517 0.2491	0.2844 0.2864	0.1458 0.3634
0.4	0.2280 0.0955	0.3405 0.2553	0.2840 0.2867	0.1474 0.3625
0.5	0.2373 0.0904	0.3296 0.2613	0.2841 0.2866	0.1490 0.3617
0.6	0.2451 0.0860	0.3198 0.2668	0.2847 0.2863	0.1504 0.3609
0.7	0.2511 0.0827	0.3113 0.2715	0.2861 0.2855	0.1515 0.3603
0.8	0.2552 0.0804	0.3044 0.2753	0.2882 0.2844	0.1522 0.3599

0.9	0.2576	0.2988	0.2910	0.1526
	0.0791	0.2784	0.2828	0.3596
1.0	0.2583	0.2945	0.2945	0.1528
	0.0787	0.2808	0.2808	0.3596

Table 2.1. (continued)

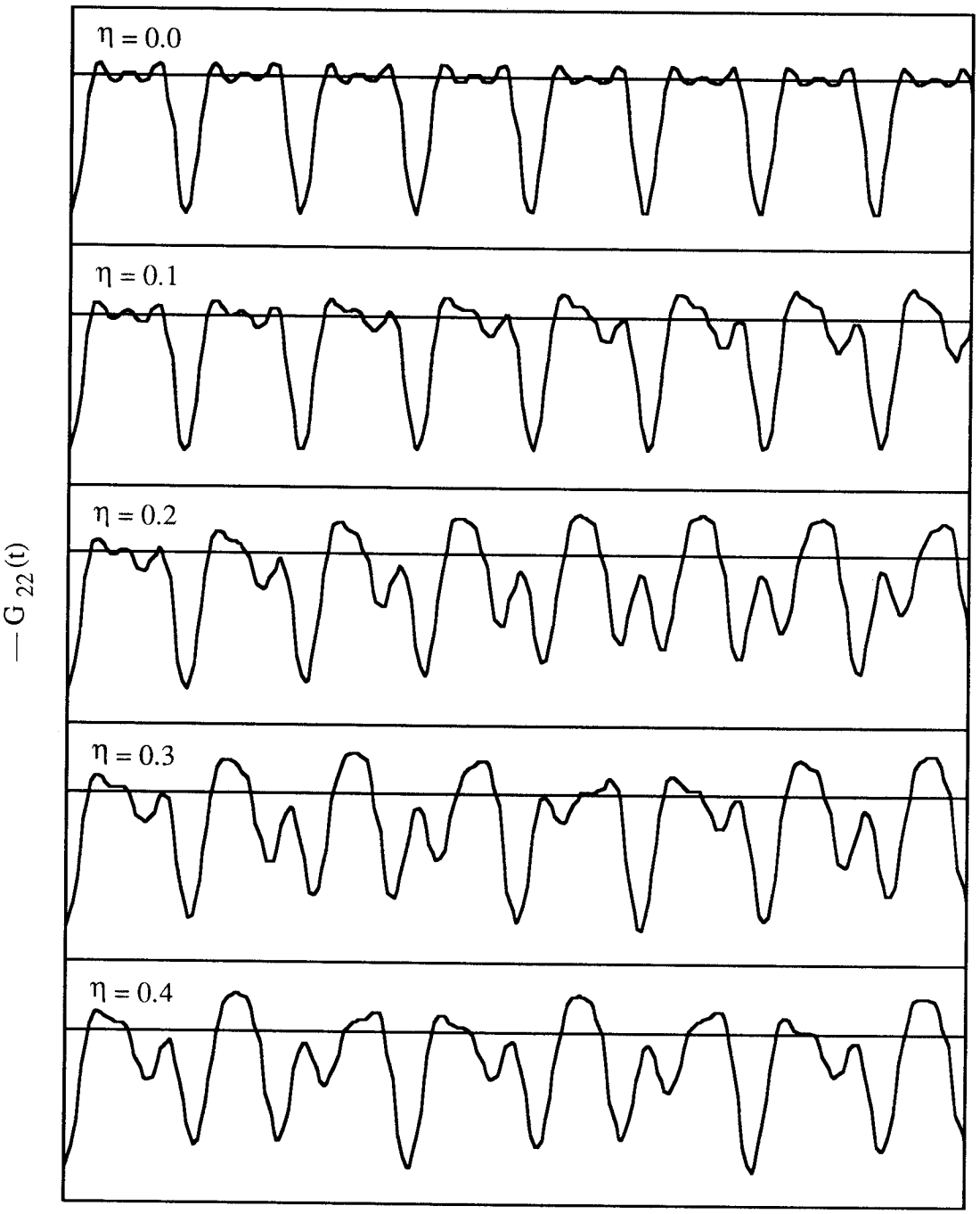

Fig. 2.2. Theoretical $G_{22}(t)$ for a static H_{QI} with I = 5/2 as a function of η.

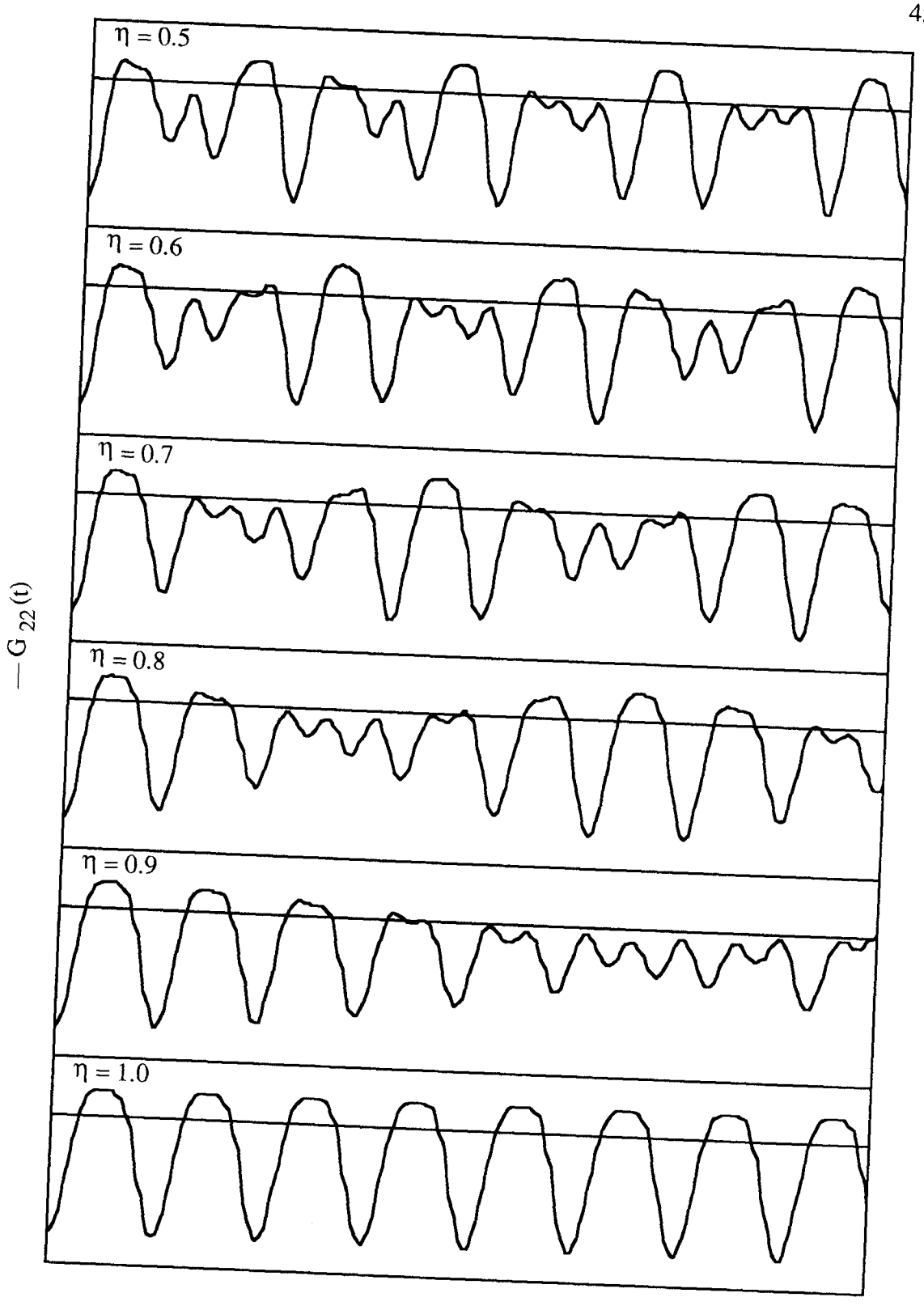

Fig. 2.2. (continued)

$$G^0_{k\,k}(t) = \int d\omega\, G_{k\,k}(t)\, P(\omega - \omega_0) \qquad (2\text{-}75)$$

with the superscript "0" in the$G^0_{k\,k}(t)$ denotes that it is the convoluted perturbation function. In the case of a Gaussian distribution, (2-70) becomes convoluted with

$$P(\omega - \omega_0) = \frac{1}{\sqrt{2\pi}\,\sigma} \exp\left\{ -\left[\frac{(\omega - \omega_0)}{\sqrt{2}\,\sigma} \right]^2 \right\} \qquad (2\text{-}76)$$

where ω_0 is the peak frequency and σ is the distribution width or standard deviation. The result of this convolution is :

$$G^0_{k\,k}(t) = S_{k\,0}(\eta) + \sum_{n=1}^{3} S_{k\,n}(\eta) \cos\left[\, \omega^0_n(\eta)\, t \,\right] \exp\left[-\frac{\left(\delta\omega^0_n t\right)^2}{2} \right] \qquad (2\text{-}77)$$

In the case of a Lorentzian distribution (2-70) is convoluted with:

$$P(\omega - \omega_0) = \frac{1}{\pi} \frac{\sigma}{\sigma^2 + (\omega - \omega_0)^2} \qquad (2\text{-}78)$$

and yields to the result :

$$G^0_{k\,k}(t) = S_{k\,0}(\eta) + \sum_{n=1}^{3} S_{k\,n}(\eta) \cos\left[\, \omega^0_n(\eta)\, t \,\right] \exp\left[-(\delta\omega^0_n t) \right] \qquad (2\text{-}79)$$

In both cases, the **relative width of the frequency distribution is defined as** $\delta = \sigma/\omega_0$. The superscript "0" in the frequencies denotes that those quantities are the peak frequencies which

are usually obtained from computer fits to the experimental data. It can be seen in (2-77) and (2-79), that due to the line-broadening the theoretical perturbation function is found to be multiplied by additional damping terms. Owing to these damping terms the higher frequency terms, ω_2 and ω_3, damp out faster than the lower frequency ω_1 term.

2.2.4 Time dependent perturbations

It should be mentioned that in the case of a time dependent electric quadrupole interaction taking place in a liquid, the correlation function can be described by (2-80) :

$$W(\theta,t) = \sum_{k_1 k_2} A_{k_1}(1) A_{k_2}(2) G^{00}_{k_1 k_2}(t) P_{k_2}(\cos\theta) \qquad (2\text{-}80)$$

with $k_1=k_2=k$ and G_{kk} being

$$G_{kk}(t) = e^{-\lambda_k t} \qquad (2\text{-}81)$$

The relaxation constant λ_r is defined as :

$$\lambda_r = \tfrac{3}{5}\tau_c < \omega_Q{}^2 > r(r+1)[4I(I+1) - r(r+1) - 1] \qquad (2\text{–}82)$$

including the relaxation time τ_c describing the time required for local configurations to change in a liquid and $< \omega_Q{}^2 >$, which is the time and spatial average of the square of the quadrupole frequency. The letter r indicates sublevels of I. For small values of λ_r, $G_{kk}(t)$ is equal to one and the correlation function, as can be seen in (2-80), is approximately a constant for small ranges of time. An example might illustrate the usefulness of this result :

In this work $YBa_2Cu_3O_{7-x}$ was investigated at temperatures higher than its melting point. The A_2G_2 of the powder, consisting of non-melted Y_2BaCuO_5 and melted $YBa_2Cu_3O_{7-x}$ is a superposition of two fractions: An A_2G_2 due to static quadrupole interaction of ^{111}In in

Y_2BaCuO_5 and a constant A_2G_2 term due to ^{111}In exposed to a fast fluctuating EFG in a metallic liquid.

Another important aspect concerned with temperature dependent, fluctuating EFG's arises from the question of how to describe the dynamics of the phase transition of $YBa_2Cu_3O_{7-x}$ from orthorhombic to tetragonal. It is assumed that due to the oxygen jumps from the O(4) site to the O(5) site and vice versa (see chapter 1.2), ^{111}In is subjected to fluctuating field gradients, flipping between a- and b-direction. Based on the experience gained from developing the xyz+z model, a model in which the symmetry axis of an axial EFG is allowed to fluctuate among orientations along x, y, and z axes in addition to a static axial EFG oriented along the z axis, it can be said that a model describing the rapid reorientation of the a and b axes will include additional damping terms in the general expression for A_2G_2.

3. Experimental arrangements

3.1. PAC spectrometer

The conventional γ–γ PAC spectrometer set up is used to detect the two correlated gamma-rays emitted by a tracer nucleus and simultaneously determine the time separation between them. As displayed in the functional block diagram in fig.3.1, four coplanar detectors are positioned 90 degrees apart from each other, surrounding the radiating sample in the center. Each detector provides two signals for every absorbed photon, one being the dynode signal (used to get energy information), the other one being the anode signal (used to get timing information). The timing signal is connected to the time the gamma–ray enters the detector and the energy signal is proportional to the energy that the gamma–ray deposited in the scintillation crystal.

3.1.1. Coincidence electronics

The timing signals from the detector 0 and detector 1 are gathered in a signal mixer before they are connected to a constant–fraction–discriminator (CFD) [EG&G Ortec, model 583]. If the time signals exceed the threshold of the CFD a start input enters the time-to-amplitude (TAC) module [EG&G Ortec, model 566]. Time pulses of detectors 2 and 3 are connected to a different mixer, delayed for a certain amount of time to let prompt events appear near the mid-range of the TAC, and after being passed thru the CFD, enter the TAC to give a stop input.

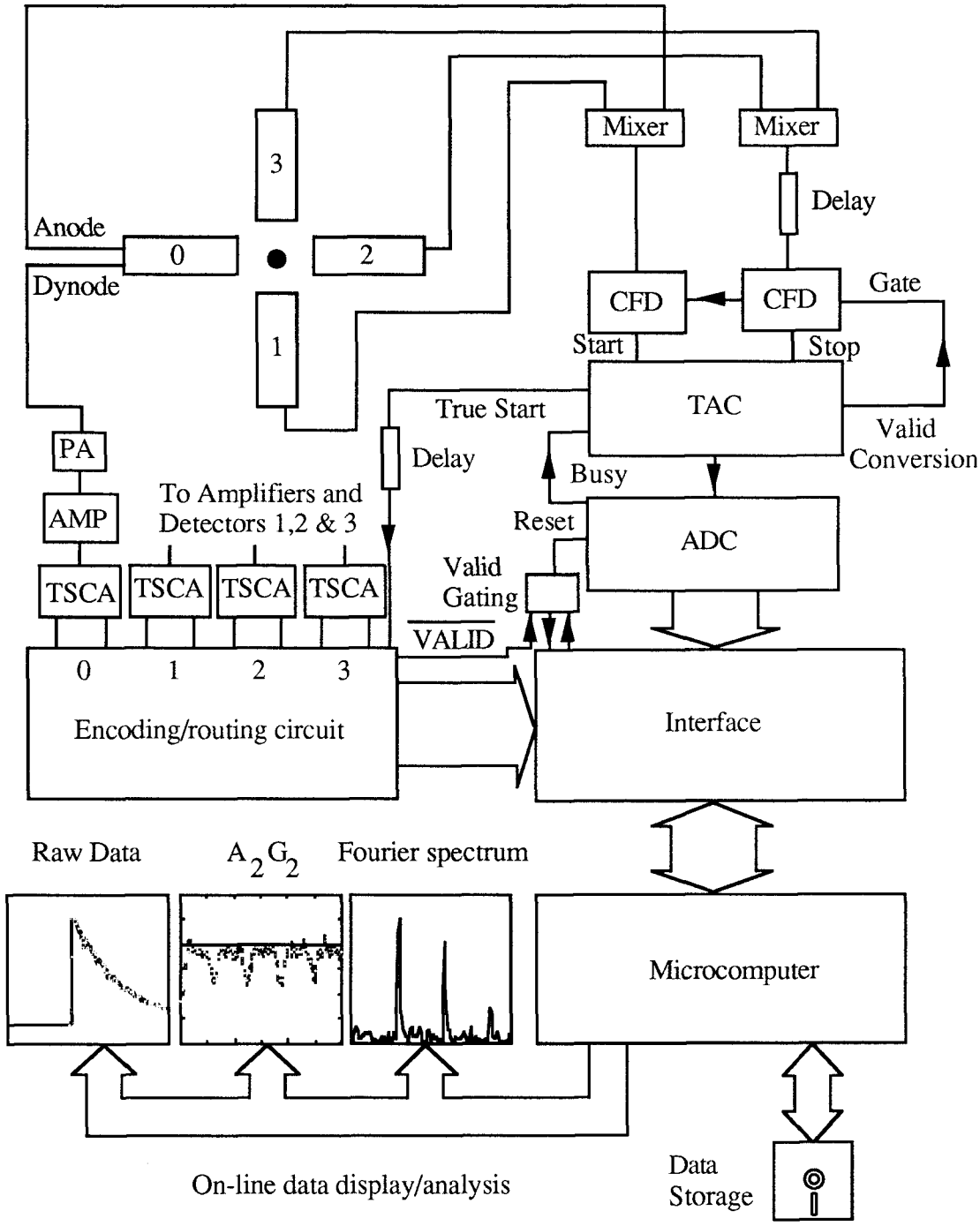

Fig. 3.1. Functional block diagram of the PAC spectrometer.

A gating mechanism at the CFDs prohibits further signal input to the TAC before the conversion is complete. An unipolar linear pulse, proportional to the time interval between "Start" and "Stop" input, is generated by the TAC and digitized by an ADC [EG&G Ortec, model 800]. For the time the ADC needs to digitize, the TAC gets a busy signal. The ADC time information, if declared valid, is then read into the Tandy/Radio Shack Color Computer.

The energy pulses from each detector are shaped and amplified by its own preamplifier and linear amplifier. A laboratory–built twin single–channel–analyzer (TSCA) is adjusted to detect the two energies, γ_1 and γ_2, from the incoming bipolar pulses. The two energy signals from each TSCA are fed into a laboratory-built encoding/routing circuit to determine the sequence of the correlated events. The encoding/routing circuit is designed such that the simultaneous detection of more than one start and/or stop event is considered invalid.

A conversion is accepted as a valid "normal" event only if a TSCA of detector 0 or 1 indicates a γ_1 was absorbed and a TSCA of detector 2 or 3 indicates a γ_2 was absorbed. If a γ_2 detected by detector 0 or 1 and γ_1 is detected by detector 2 or 3 then it is called a valid "reverse" event. As soon as a valid event is flagged, the computer is interrupted and the digitized time separation of the two cascade gamma–rays and the sequence of detection of an event (routing information) is collected by the interrupt service routine of the operating software and stored in the proper location of the computer memory. While the experiment is in progress, the computer can also be used for displaying the raw data on an oscilloscope and the calculated $A_2G_2(t)$ function on the screen. To prevent loss of data due to power failure or computer crashes, the data should be saved as often as possible.

3.1.2. Operating software

A Tandy/Radio Shack Color Computer, tenderly called CoCo, is used to control the spectrometer and store the results on the disk. The coincidence electronics is connected to the CoCo via a bus expansion box [Basic Technology, Ortenville, MI, model BT 1000] by use of a

peripheral interface adapter (PIA) chip [Synertek, Santa Clara, CA, type SY 6522]. Most of the spectrometer software is written in BASIC, but the time–critical parts are written in machine language. The most time–critical part is the interrupt service routine, because the time spent in reading the PIA ports largely determines the dead–time of the system. On entry of the interrupt service routine, the processor register, status and return address are saved on the stack. After the PIA registers are read, the ADC is reset and the next interrupts can occur while the computer is still processing the previous one. This sets an upper limit on the rate which interrupts can be accepted. If the interrupt rate becomes too high, the stack overflows and the computer crashes. In practice, this has not been a problem since the activity of the sample is controlled through the sample making process. An interrupt service routine examines the VALID bit (most significant bit of the routing information) and returns immediately from interrupt if the event is invalid . In the case of a valid interrupt, a memory location is decided from the data received from the PIA input lines.

The computer's random access memory (RAM) is divided into 16 sectors corresponding to the pairs of detectors that detected γ_1 and γ_2. For example, sector 0/2 holds the spectrum of events for which γ_1 is detected in detector 0 and γ_2 in detector 2, etc. Each sector consists of 512 channels and each channel is represented by two bytes. The routing information identifies the memory sector, while the ADC conversion result designates the offset of a particular event in that sector. As soon as the channel which corresponds to the detected events is identified the count in that channel is increased by one and the routine returns from interrupt. The channel representing time–zero (of a prompt event) is located near mid–range of the TAC (channel 256), so that in addition to the "normal" spectra coming from the sectors 0/2, 0/3, 1/2 and 1/3, the "reverse" spectra,due to information stored in sectors 2/0, 3/0, 2/1 and 3/1 can be accumulated. For a typical run, about 5×10^4 to 6×10^4 counts per channel at the peak of the spectrum are accumulated. A typical run takes 8 to 24 hours to accumulate two statistically independent spectra ("normal" and "reverse"). When sufficient data have been collected, the spectra and relevant information such as sample name, date, temperature

and calibration data are saved to a floppy disk for later analysis on a Apple Macintosh II computer.

3.1.3. Spectrometer calibration

If an experiment is performed, one of the routine tasks to fulfill is the adjustment of the so called energy -windows at the TSCA's. With the help of a multichannel analyzer (MCA) an energy spectrum of the current sample is obtained. The locations of the two gamma peaks, are noted and the TSCA is adjusted so that it cuts out the right energies, namely the 171 keV(γ_1) or 245 keV(γ_2) peak for detection. The task of the time calibration consists of three parts: (i) the lengths in the time signal cables are adjusted such that the time–zero channels for all memory sectors are the same, (ii) the time scale of the TAC and (iii) the time resolution of the spectrometer have to be determined. Before a time calibration is performed, the energy windows of the TSCA must be adjusted very carefully to correspond to the ^{111}In/^{111}Cd tracer energy peaks. The time–zero channel for a prompt event in each memory is aligned using a ^{22}Na source. The 2.6 yrs half–life ^{22}Na decays through β^+ emission process to its daughter isotope ^{22}Ne. The positron eventually annihilates with a electron in the surrounding material. In most of the cases two photons, each with energy of 511 keV, are created simultaneously and emitted in opposite directions. Occasionally, the photon pair will be absorbed by two detectors and the resulting prompt spectrum accumulated in the corresponding memory sector ideally should resemble a delta–function. In reality, the prompt peaks have a Gaussian–like distribution due to the finite time resolution of the spectrometer. By adjusting variable delay lines between the Mixers and CFDs, the time–zero channels of all memory sectors are aligned to within a few tenths of a channel width. Owing to the fact that two 511 keV photons always travel in opposite direction, the prompt peaks for the 90° degree angle detector pairs are accumulated through physically swapping the "start" detectors 0 and 1. After prompt peaks for each detector pair have been accumulated for the same time interval, a program determines location and full width at half maximum (FWHM)

for every prompt peak and computes the instrumental resolution function for both the normal and reverse spectrum. The instrumental resolution function, used during data analysis to account for the finite time resolution of the spectrometer, is the sum of the prompt peaks in each of the four channels before and after the time–zero channel and is normalized to 255 in the time–zero channel itself. Special care needs to be taken to ensure that the prompt peak counts for each detector pair are as close as possible in order to get a statistically equal weighted contribution from each pair. The FWHM of the resolution function is as wide as the prompt peak belonging to the worst detector pair, assuming that the prompt peaks are lined up perfectly.

The FWHM of the spectrometer used in this work is about 2 channels. with a resolution of 1.6 ns per channel the overall time resolution is around 3.2 ns. A time calibrator (EG & G Ortec model 462) is used to determine the absolute time scale of the TAC. The time calibrator generates Start and Stop pulses separated by integer multiples of a chosen constant period. These peaks are fed directly into the TAC inputs, and a calibration program accumulates the periodic repeating peaks and evaluates the time calibration by doing a least square fit. The time calibration gives the absolute time scale for the TAC, i.e. time per channel. The time calibration for the data collected in this work is 1.60 ns/channel with an error of less than 0.4%.

Time–zero channel, instrumental time resolution function and time calibration are stored in computer's RAM and saved with experimental spectra to a floppy disk so that this information is available when the spectra are analyzed.

3.1.4. Gamma-ray detectors

The detectors used in this work consist of 1.5" × 1.5" × 1.5" cylindrical NaI(Tl) scintillators mounted onto photomultipliers .Each detector is powered by its own high voltage power supply .

A photon entering the scintillator interacts with the material. The intensity of the resulting fluorescent light is proportional to the energy the photon deposited in the scintillator. The fluorescence light then enters the window of the photomultiplier and hits the cathode which is coated with photoelectric material and frees electrons which are then accelerated and multiplied along the dynode chain. In using γ-γ TDPAC techniques to probe microscopic properties of condensed matter, a set of scintillators with both good energy and timing resolution is essential.

NaI(Tl) scintillators have a high efficiency and good energy resolution but a rather mundane time resolution—mostly in 2 to 3 ns range. Since NaI is hygroscopic , it is kept sealed to exclude reactions with water vapor. The sealed crystals have a window at the end which is coupled to the photomultiplier by some optical grease. The detectors are covered with magnetic shielding to shield off the external magnetic field. All four detectors are attached to aluminum frames and are free to slide along tracks at 90° angles from each other. A ruler at the side of each detector provides information about the sample–detector distances.

3.1.5 Furnace arrangement

When the high-temperature furnace was designed, the following constraints applied to it: (i) The outer surfaces of the furnace must be at room temperature so that detectors work at the same temperature independent of the sample temperature. (ii) The furnace body should be thin and constructed using a low Z material so as not to reduce the intensity of the gamma-rays emitted by the sample significantly. (iii) The furnace must work reliably at 1400 ℃ or even higher continuously over several weeks. The furnace used in this work, is built around a closed-one-end alumina furnace tube (McDanel Refractory Co.,Beaver Falls, PA, type 998) with an inner diameter of

3/8" and an outside diameter of 1/2". The heating element is cut from a 0.005" thick graphite foil with the help of a predrawn paper pattern (fig. 3.2a.). The heating element is wrapped around the furnace tube and covered with one layer of organic binder free alumina thermal insulation and two layers of zirconium foil. The zirconium foil serves two purposes: heat shielding, and oxygen getter to prevent the heating element from oxidizing. Two pieces of copper foil are used as the current leads which are connected to the vacuum fit-through. The heating unit is mounted in a aluminum housing surrounded by a water-cooled jacket (fig. 3.2b.). A laboratory-built AC power supply is used to power the furnace. The open end of the furnace tube is exposed to the air, and the sample and a Pt-Pt/10%Rh thermocouple is placed in the center of the tube. The temperature is controlled by a proportional controller (Omega Engineering, Stamford CT, model 49) connected to the thermocouple. It was found that a moderate vacuum which can be achieved by a mechanical forepump is sufficient to prevent the heating element from oxidizing. A well-constructed furnace typically will last for 3-6 months under normal operation up to 1400°C.

Temperature profiles of the furnace have been measured over various temperatures up to 1400°C [54]. The temperature differences between all sides of a sample was found slightly less than 10° C at 1400°C.

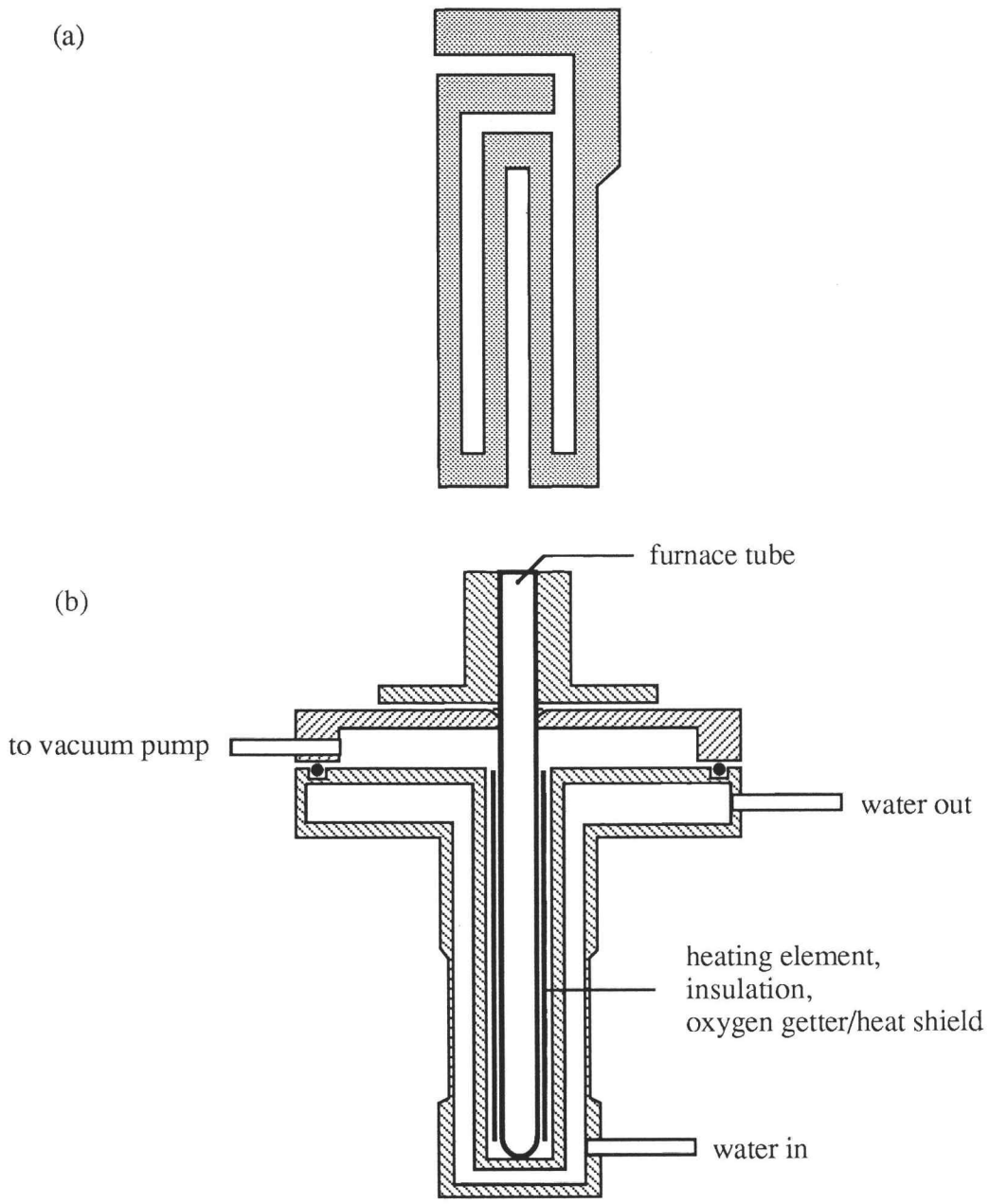

Fig. 3.2. (a) The graphite foil heating element and (b) sectional view of the PAC furnace. The resistance of the graphite heating elements is ~4Ω.

4. Data reduction and analysis

The following steps are involved in the process of data evaluation:

1. The raw data, consisting of counted decay events and calibration information are saved to a floppy disc by the Coco.
2. This information is read into an IBM, which calculates $A_2G_2(t)$, which is the experimental perturbation function $G_2(t)$ multiplied by the effective anisotropy A_2.
3. Raw data and $A_2G_2(t)$ are now transferred to an Apple Mcintosh II computer. The experimentalist can now make use of the following laboratory built programs:
   - 3a. look at the raw data to check whether the alignment of the time zero channels has changed during the run. This is easily possible due to temperature changes in the laboratory.
   - 3b. take the Fourier transform of the experimental $A_2G_2(t)$ to get a rough idea about the number of unequivalent probe sites and the corresponding PAC frequencies.
   - 3c. fit the experimental $A_2G_2(t)$ to different models
   - 3d. take the Fourier transform of the fitted $A_2G_2(t)$ function to check how accurate and complete the fit is.

The block diagram [54] in fig. 4.1. illustrates the data reduction process :

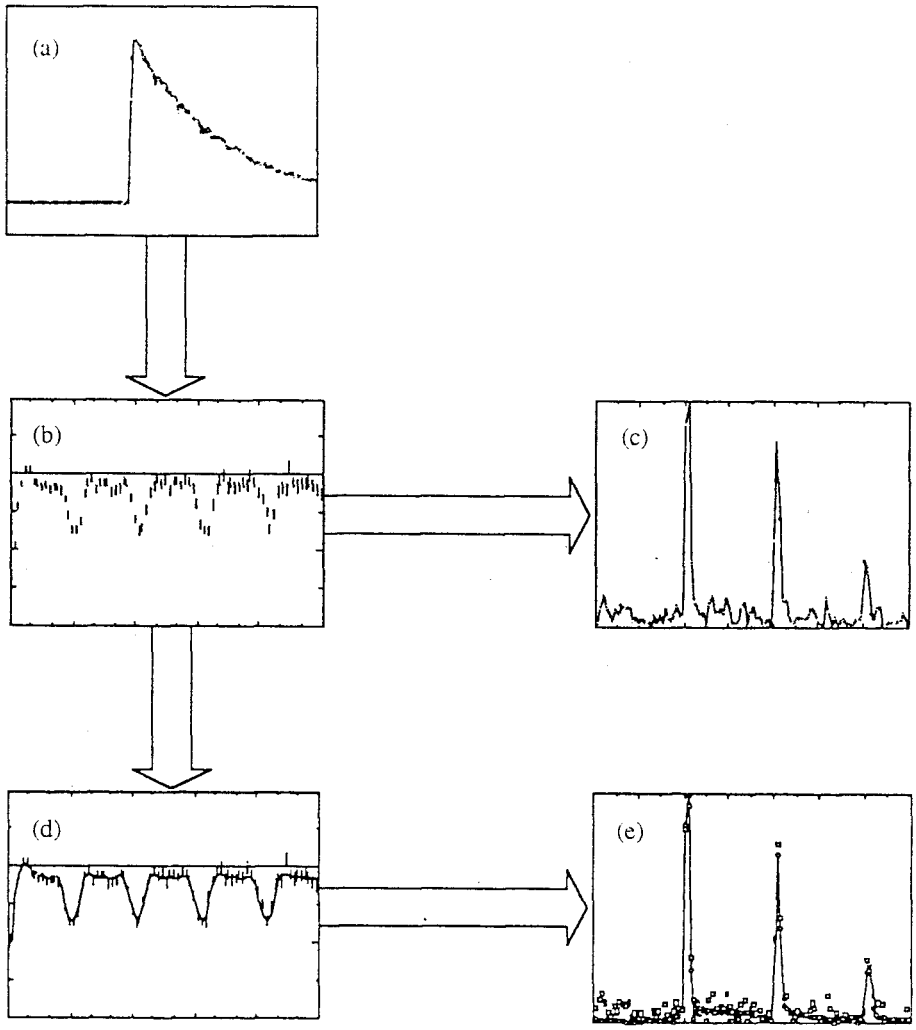

Fig. 4.1. The experimental $A_2G_2(t)$ (b) is computed from the background corrected coincident counts for a 90° and 180° detector pair, which is illustrated in (a). (c) the Fourier transform of (b) is performed to obtain a rough estimation of the PAC frequencies and number of possible sites. The computer fit to (b) is attempted and the time domain fit (d) and Fourier transforms for the fitted function and experimental $A_2G_2(t)$ (e) are compared.

For each detector pair i/j, the raw data contained in the corresponding memory sector i/j have the following form :

$$D_{ij}(\theta,t) = \frac{1}{\tau_N} e^{-\frac{t}{\tau_N}} e_i e_j N_0 W(\theta,t) + B_{ij} \qquad (4\text{–}1)$$

Subtracting the average background Bij from (4-1), the event counting rate Cij becomes :

$$C_{ij}(\theta,t) = D_{ij} - B_{ij} = \frac{1}{\tau_N} e^{-\frac{t}{\tau_N}} e_i e_j N_0 W(\theta,t) \qquad (4\text{–}2)$$

The angle θ describes the angular separation between the ith and jth detector, e.g., the angle between detector 0 and 2 is 180°, etc., and e_i, e_j are the detectors' efficiency. N_o is the decay rate of the parent isotope (in this case, ^{111}In) and τ_N is the mean life of the intermediate state ($5/2^+$ state of the ^{111}Cd, τ_N=85ns). $W(\theta,t)$ is the angular correlation function which contains all the information about the interaction of the probe and the environment. The background counts are taken from channels that correspond to the events which happened 160 to 320 ns before the time–zero.

As mentioned in chapter 2.2.2., equation (2-74), the angular correlation function for static interaction in a polycrystalline sample is described by :

$$W(\theta,t) \approx 1 + A_2 G_2(t) P_2(\cos\theta) \qquad (4.3)$$

with the approximation $A_{44} \approx 0$. If this is inserted in equation (4-2) and written out for each detector combination, the following spectra–ratios for the normal (4-4)- and reverse (4-5) spectrum can be defined [64] :

$$R_n(t) = 2\frac{(C_{02}\,C_{13})^{1/2} - (C_{03}\,C_{12})^{1/2}}{(C_{02}\,C_{13})^{1/2} + 2(C_{03}\,C_{12})^{1/2}} \qquad (4\text{–}4)$$

$$R_r(t) = 2\frac{(C_{20}\,C_{31})^{1/2} - (C_{30}\,C_{21})^{1/2}}{(C_{20}\,C_{31})^{1/2} + 2(C_{30}\,C_{21})^{1/2}} \qquad (4\text{–}5)$$

Under the assumption that the detector single efficiency is the same for each detector, the so defined spectra–ratios are approximately equal to $A_2G_2(t)$, the product of experimental perturbation function $G_2(t)$ and effective anisotropie A_2.

4.1 Fourier transformation

For a fast Fourier transformation (FFT) of the $A_2G_2(t)$, the time–domain data were multiplied by a time–domain window to reduce the spurious peaks in the Fourier spectrum due to the finite extension of the data. The windowed time data were reflected to negative time to increase the data range. A cosine window, which proved to have the best balance in producing narrowest main peaks and smallest sidelobes, was used in finding the FT for the $A_2G_2(t)$ function throughout this work.

4.2. Fitted and derived PAC parameters

A nonlinear least–squares fitting routine [65] was used to fit the experimental $A_2G_2(t)$ function. In the fitting routine, an appropriate theoretical expression of the $A_2G_2(t)$ function is convoluted with the system time resolution function to account for the finite instrumental resolution of the spectrometer, and with a Lorentzian distribution to account for the distribution of the EFG. If a meaningful fit is obtained, the card with the fitted parameter and the corresponding plot to the fitted function can be saved and/or printed out. An example of these cards is presented in fig. 4.2. .

Fit ID: HTCRO-SR T=1025 C | Copy | Save | New Fit | Function 16

A2	[none]	-.110299	.113862	0.00189
T0 Channel	[none]	6.44657	6.64883	.152936
Omega 1 [1]	Mrad/sec	55.4852	54.3254	.775209
Omega 2 [1]	Mrad/sec	99.8922	99.1149	1.01229
Delta [1]	%	1.00000	1.00000	0
Fraction [2]	%	29.3896	26.3152	1.14008
Omega 1 [2]	Mrad/sec	16.0592	16.3863	.641458
Omega 2 [2]	Mrad/sec	31.0438	30.1507	1.09643
Delta[2]	%	0	0	0
Fraction [3]	%	31.3482	35.2003	1.47362
Omega 1 [3]	Mrad/sec	141.517	141.931	.542663
Omega 2 [3]	Mrad/sec	-2	-2	0
Delta[3]	%	2.00000	2.00000	0
Fraction [4]	%	20.4789	20.1225	1.99802
Omega 1 [4]	Mrad/sec	469.124	460.421	2.16233
Omega 2 [4]	Mrad/sec	799.391	808.949	6.57350
Delta [4]	%	1.00000	1.00000	0
Fraction [cubic]	%	0	0	0
		0	0	0
		0	0	0

*aftereffects terms

Chi Squared = 1.10127 Fit from data point 6 to 195

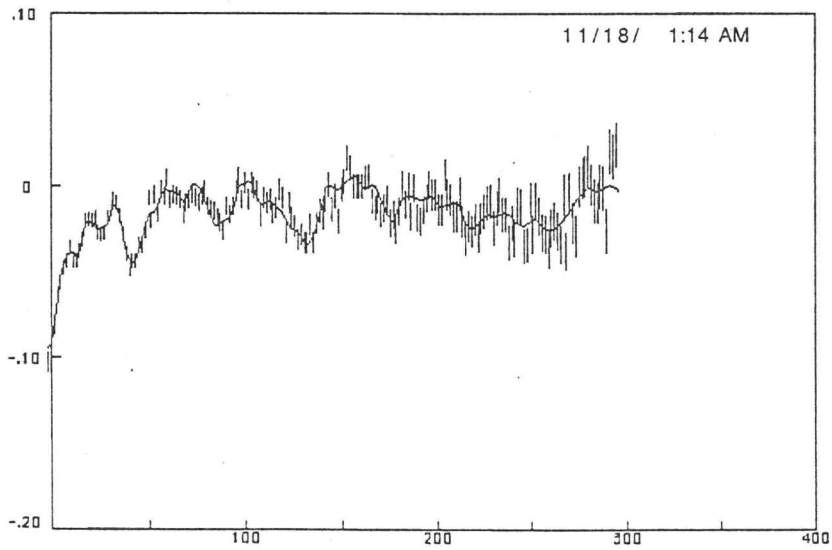

Fig. 4.2. Fitting card used in this work.

The parameters encountered on this card are :

A_2^{eff}: observed effective ansiotropy, i.e. the true A_2 reduced by solid angle correction factor and by other known or unknown sources.

To : If the time zero channel has shifted slightly, but by the same amount for each detector pair, a change in To can shift the $A_2G_2(t)$ back to the channel for which the calibration has been made.

ω_1, ω_2 : PAC frequencies, which depend on the strength of the interaction between the nuclear quadrupole moment and the EFG due to the environment and asymmetry of the EFG.

δ : relative distribution of the EFG, $\delta = \frac{\Delta\omega}{\omega}$, also called the line-width describes the quality of the sample. A broadening in delta can indicate that a certain model is not appropriate anymore.

f_i : fractional weight of the ith site, $\Sigma f_i = 1$.

When ω_1 and ω_2 are established the following quantities can be deduced:

a) $\omega_3 = \omega_1 + \omega_2$

b) the magnitude of the electric field gradient V_{zz} (see formula (2-55)). A modification of V_{zz} has to be taken into account since it is found that the observed nuclear quadrupole interaction is enhanced due to distortions in the closed electronic shell of the probe atom due to external electric fields. For a cadmium probe, the observed electric field gradient magnitude V_{zz} can be parameterized as [66] :

$$V_{zz} = (1 - \gamma_\infty) V_{zz}(lat) \qquad (4\text{-}6)$$

where $V_{zz}(lat)$ is the EFG due to ion cores in the lattice or the lattice EFG, and γ_∞ is the Sternheimer antishielding factor which is negative for most ions. A rather complete tabulation of γ_∞ for closed-shell ions, calculated using a relativistic Hartree–Fock–Slater

electron theory, can be found in the literature [67]. For the Cd^{2+} ion, the γ_∞ is –29.27.

d) the asymmetry parameter η . For electric field gradients due to an axially symmetric lattice we have $\eta = 0$, while for sites with lower symmetry $0 \leq \eta \leq 1$ applies.

4.3. The effective anisotropy A_2^{eff} for ^{111}Cd

It should be mentioned that the theoretical value of A_2, only depending on the spins of the nuclear levels and multipolarities of the radiations involved in the decaying process and therefore independent of the environment of the probe atom, in the experiment becomes modified to :

$$A_2^{eff} = \gamma_a\gamma_b\gamma_c\gamma_d\gamma_e A_2 \qquad (4\text{–}7)$$

The five multiplying factors in front of the negative A_2 have the following meaning:

(i) finite size attenuation (γ_a) – The measured anisotropy is an average quantity, since real samples and detectors have finite size.

(ii) finite time resolution attenuation (γ_b) – the finite time resolution of the spectrometer causes the observed spectrum to be a convolution of the true spectrum and system resolution function. In the literature, a Gaussian shape spread is often assumed for the system resolution function [68].

(iii) Compton scattering (γ_c) – due to placing the samples in the previous described PAC furnace, the gamma–rays need to penetrate layers of materials before they reach the scintillator. The apparent detection angle of the detector is increased, as the gamma–rays are scattered through small angles without significantly losing their energy.

(iv) sample self–absorption [69] (γ_d)– This happens most often for high Z samples. In these types of samples the gamma–ray

cascades travel in the 180° direction is more likely to be absorbed than those of in the 90° direction, especially for events that occur near the surface.

(v) unknown source factor (γ_e)– the correction factor for all unknown sources

The effective anisotropy A_2^{eff} is the value of $A_2G_2(t)$ at the time t = 0, since G(t=0) = 1 and therefore appears right at the beginning of the $A_2G_2(t)$ plot. Experimental runs with different samples, but same detector distance and similar activity, should result in similar A_2^{eff} values. The further the detectors are away from the center, the larger the negative amount of A_2^{eff}. The ideal value of A_2 is -0.180(2).

5. Review of PAC results on $YBa_2Cu_3O_{7-x}$ and other related compounds

5.1. PAC spectroscopy on $YBa_2Cu_3O_{7-x}$

Several groups [70-77] have attempted PAC measurements on $YBa_2Cu_3O_{7-x}$. Most of them [70-75] used ^{111}In as the nuclear tracer, although W.Shen et al. [76] worked with ^{111}Ag and Z. Akselrod et al. [77] explored ^{181}Ta. Different techniques were used to incorporate the ^{111}In probe:

- Implantation of ^{111}In at 400 keV into polycrystalline $YBa_2Cu_3O_{7-x}$ and single crystal $YBa_2Cu_3O_{7-x}$. Annealing of the radiation damage in air at temperatures as high as 650°C and restoring the orthorhombic phase through annealing in O_2 of 400mbar at 500°C [70,71].

- Drying ^{111}In, obtained as an acid $InCl_3$ solution, and than evaporating onto $YBa_2Cu_3O_{7-x}$ samples which were annealed at 970°C for two hours in an O_2 atmosphere and slowly cooled down [72].

- Diffusing ^{111}In onto $YBa_2Cu_3O_{7-x}$ at 830°C for 15 hours and cooling slowly over a period of 12 hours in flowing oxygen [73].

- Stoichiometric mixtures of CuO, $BaCO_3$ and Y_2O_3 and In_2O_3 to prepare $YBa_2(Cu_{1-x}In_x)_3O_{7-y}$ with x=0.01, 0.03, 0.05 were synthesized and pressed into pellets, sintered in air flow for 17 hours at 900°C and then slowly cooled down [74].

- Variety of techniques (not explained further). Calcination in air at 750°C in O_2 [75].

Most of them report about difficulties in substituting ^{111}In into the $YBa_2Cu_3O_{7-x}$ crystal-lattice and obtaining reproducible results. Based on the measured PAC results, point-ion model calculations and chemical considerations, all interpretations [70-75] consider either a

Yttrium- or Copper-site substitution. Table 5.1 summarizes published results on $YBa_2Cu_3O_{7-x}$.

Table 5.1 PAC parameters and their site assignment as measured at room-temperature by other groups.

ω_1	ω_2	η	δ	interpretation	reference
[10^{-6} rad/sec]					
126	252	0	2	Cu-1 site in the	70
126	252	0	110	tetragonal phase	
237	237	1	10	Cu-1 site in the	70
256	256	1	10	orthorhom. phase	70
147	294	0	12	Cu-1 site with 3 oxygen atoms	70
246	246	1	?	Cu-1 site in the orthorhom. phase	73
56	104	0.25	?	Cu-1 site in the tetragonal phase	73
42	73	0.37	?	Y-site	72
116	198	0.37	?	Y-site	75
144	187	0.7	?	suggest copper-	74
154	278	0.29	?	sites	74

5.2. PAC spectroscopy on compounds related by the chemistry of processing $YBa_2Cu_3O_{7-x}$

In the process of preparing a sample, small percentages of second phases and starting materials are encountered in the end-product $YBa_2Cu_3O_{7-x}$. In the course of this work it was found that 211 incorporates the tracer ^{111}In more easily than 123 does. For that reason, depending on the sample making conditions, a high fraction due to ^{111}In at a 211 site can be detected despite the fact that the total quantity of 211 is less than 5%. Other secondary compounds like $BaCuO_2$, CuO, Cu_2O, Y_2O_3, In_2O_3 and $Y_2Cu_2O_5$ might also have higher distribution coefficients for ^{111}In than $YBa_2Cu_3O_{7-x}$ does. It is necessary to exclude PAC frequencies resulting from these second phases when interpreting the $YBa_2Cu_3O_{7-x}$ spectrum. PAC investigations done on the described materials are summarized in table 5.2 .

Table 5.2 PAC parameters found on investigations of Y_2O_3, In_2O_3, Cu_2O, CuO, Y_2BaCuO_5, $Y_2Cu_2O_5$.

material	f	ω_1	ω_2	η	δ	T[°C]	reference
		[10^{-6} rad/sec]					
Y_2O_3	51	138	276	0	10	23*	71
	11	95	124	0.7	4		
	38	50	100	0	48		
	77.3	133	167	0.73	0.93	1200	54
	22.7	148	292	0.02	0.2		

material	f	ω_1	ω_2	η	δ	T[°C]	reference
		[10^{-6} rad/sec]					
In_2O_3	75	160	202	0.72	0	-250 to	78
	25	148	290	0.12	0	750	
	72.3	160	208	0.69	0.48	1000	53
	27.7	147	291	0.04	0.57		
	75	160	208	0.69	4	23*	71
	25	145	290	0	4		
Cu_2O	78	257	399	0.49	15	23	79
	22	145	173	0.79	4		
	81	235	425	0.29	2	400	79
	19	139	167	0.78	4		
	85	243	418	0.36	30	500	79
	15	160	162	0.98	22		
	89	210	404	0.18	30	700	79
	11	115	158	0.63	5		
	81	264	390	0.55	24	780	79
	19	155	155	1	13		
	95	212	366	0.36	53	900	79
	5	114	146	0.7	4		
	100	116	232	0	3	23*	71

Table 5.2. (continued)

material	f	ω_1	ω_2	η	δ	T[°C]	reference
		[10^{-6} rad/sec]					
CuO	81	222	339	0.51	19	23	79
	19	117	169	0.57	5		
	81	217	312	0.58	15	500	79
	19	119	151	0.72	3		
	50	468	766	0.42	3	23*	71
Y_2BaCuO_5	?	62	113	0.28	7	23*	71
	?	215	423	0.12	10		
Y_2BaCuO_5	app. 60%	62	113	0.28	?	23*	70
		99	160	0.44	?		
	?	222	424	0.19	?		
$Y_2Cu_2O_5$	same as seen on Cu-1 site in $YBa_2Cu_3O_{7-x}$ in ref.70, (same author)						80

* indicates that the temperature of the measurement wasn't mentioned explicitly.

Table 5.2. (continued)

6. Sample preparation

One of the major difficulties in PAC experiments is to incorporate the desired radioactive tracer into the materials one wants to investigate. Before any PAC work can be done, it is essential to assure that the radioactive tracer has some solubility in the material of interest.

Three papers [83,84,85] which report about indium substitution in $YBa_2Cu_3O_{7-x}$ were reviewd. They all agree that if indium is substituted in an amount smaller or equal to 3 percent per formula unit, the crystal structure and the superconducting transition temperature of $YBa_2Cu_3O_{7-x}$ remain basically unchanged. G. Weidlich and J.Gardner [83] found their data most consistently interpreted by assuming an indium substitution at the yttrium site.

Two ways of preparing a superconducting $YBa_2Cu_3O_{7-x}$ powder, made available to our laboratory by Dr. James A. Sommers of Teledyne Wah Chang Albany (Albany, OR), were explored. One is called the nitrate evaporation method, the other sol-gel method. Most of the samples analyzed in this work are sol-gel made.

6.1 Sol-gel route to $YBa_2Cu_3O_{7-x}$

An improvement in preparing $YBa_2Cu_3O_{7-x}$ has been achieved by using this new method. The following description has been provided by Dr.Summers:

From stock nitrate solutions of Y, Ba and Cu, a master solution with cationic molar ratios of 1:2:3 was made. Crystalline ethylene diamine tetraacetic (one mole EDTA for each mole of cations, in accordance with Fransaer, et al.[81]) was stirred into this mixture, with little dissolution. Ammonium hydroxide (50 volume percent) was added dropwise until the EDTA dissolved , at pH close to 7. Such a solution had a loading of about 35 mg oxide/ml of solution. A few ml of the solution were taken to which a drop of a HCl/HNO_3 solution containing ^{111}In was added. These doped solutions were dehydrated and converted to oxides in a ceramic casserole on a hot plate. The solutions

were evaporated to yield a clear, rigid gel below 100°C. With constant stirring, the gel was further heated to drive off water, decompose the nitrate, then oxidize the organic content. The following sequence was observed: transparent blue gel → blue green crystalline mass evolving nitrogen oxides → fine brown powder with tendency toward combustion → fine black powder. Dunn et al. [82] find $BaCO_3$, CuO and Y_2O_3 by x-ray diffraction at 450° C in a similar procedure. These intermediates combine to form $YBa_2Cu_3O_{7-x}$ near 900°C . This prereacted powder of mixed oxides, which is much more uniformly mixed than the powders used in the normal solid state synthesis, is poured in an alumina sample boat, which in turn is placed in a computer-controlled furnace.

The experimentalist can now choose the firing schedule in terms of :

how fast the powder reaches the final firing temperature, how long it will remain there and how slowly the sample will be cooled down. Most of the samples in this work were heated to 850°C in 10 C/min and rested there for 10 minutes to let the overshoot relax down to 850° C. The heating was continued at a rate of 1 C/min to 940°C. The powder reacted now at its final temperature of 940°C for 12 hours. It was cooled at a rate of 1 C/min, interrupted only by a 2-hour pause at 450°Cto let the sample soak in oxygen. During all these steps the lab furnace is kept in a tilted position to allow substantial air convection. By similar means EDTA- containing solutions of CuO, BaCuO and Y_2BaCuO_5 were prepared.

6.2 Nitrate evaporation method for $YBa_2Cu_3O_{7-x}$ samples

A carefully–prepared nitrate solution with Y:Ba:Cu in the molar ratio of 1:2:3 was used as starting material. A few ml of the solution were taken to which a drop or two of the ^{111}In containing HCl solution was added. The resulting solution was absorbed into ashless burning wool and then heated in a lab alumina casserole and stirred until all liquid had evaporated and the wool carbon had burned off. The nitrate evaporation method allows to introduce the ^{111}In PAC tracer very

uniformly throughout the sample and the wool will keep the components from separating in the evaporation process. Again, the material is much more uniformly mixed than the powders used in the normal solid state synthesis. From here on the same steps as described in 6.1 apply.

6.3 Quality of the $YBa_2Cu_3O_{7-x}$ samples

The samples produced by this methods were checked and investigated by G Weidlich [83] and H.Su [54]. X-ray diffraction pattern showed the well known orthorhombic $YBa_2Cu_3O_{7-x}$ peaks with a small percentage of second phase peaks. Meissner flux exclusion experiments showed a very sharp Meissner effect with an onset at 92.7 K with a transition width smaller than 1K.

7. PAC on $YBa_2Cu_3O_{7-x}$

This chapter presents the PAC results consistently found in all the samples prepared by the sol-gel method. All $A_2G_2(t)$ spectra were fitted with the standard model for static interaction between the electric field gradient and quadrupole moment of the ^{111}In intermediate state in a randomly oriented polycrystalline sample as described in chapter 2.

7.1 The observed PAC frequencies

The measured $A_2G_2(t)$s are found to be superpositions of $A_2G_2(t)$s resulting from probe interactions at different sites in the 123-crystal structure and $A_2G_2(t)$s due to probe interactions in the second phase (211) or metallic melt. The samples differ in the fractional weight assigned to each of these $A_2G_2(t)$s. This superposition of different fractions corresponds mathematically to :

$$A_2G_2(t)=A_2^{eff}[(1-f_2-f_3-f_4-f_5-f_6-f_7)G_2^1+f_2G_2^2+f_3G_2^3+f_4G_2^4+f_5G_2^5+ + f_6G_2^6+f_7G_2^7] \qquad (7\text{-}1)$$

The f_i indicate the fractional weight of the G_2^i contributing to the total G_2 . The normalization is $\Sigma f_i = 1$. Each G_2^i is an oscillating function of time depending on the PAC frequencies ω_1^i, ω_2^i and $\omega_3^i = \omega_1^i + \omega_2^i$ as derived in formula (2-70)). For each site a Lorenzian broadening is assumed. The PAC parameters, as used in this chapter , are interpreted in the following way :

The site with fraction f_1 observed in the temperature range before the phase transition (23°- 600°C), is due to ^{111}In substitution at the yttrium site in 123. At temperatures which exceed the phase transition temperature, but are below the melting point of 123, fraction f_2, representing different PAC parameters resulting from a now different surrounding at the same site in 123, replaces fraction f_1. If the melting point is passed, 123 decomposes to 211 and a metallic liquid. Fraction

f_3 accounts for this liquid. All of the next three fractions, f_4, f_5 and f_6 have in common that they appear only to a small percentage and therefore are not free of ambiguity. The PAC parameters of fraction f_4, being observed below the phase transition temperature, have been mentioned in a paper from Uhrmacher el al. [80] as being unpublished results from Plank et al. Other runs, which have been done in the vicinity of the melting point of 123, indicate that the value of fraction f_5 increases with higher temperature, possibly due to thermally populated copper sites in 123. Fraction f_6 accounts for an observed high frequency site which couldn't fully be resolved.

A measurement performed on a sol gel prepared 211 sample confirmed that the PAC parameters of fraction f_7 are due to ^{111}In substituted in 211 sites.

7.1.1 Fitting philosophy

In the course of this work 26 $YBa_2Cu_3O_{7-x}$ samples were investigated and lots of fits have been performed to find the most consistent results. The maximum amount of sites used in fits was five, four static sites and a liquid site (see fig. 4.2). The errors in the PAC parameters f_i, $\omega_1 i$, $\omega_2 i$ and δi depend on several things :

i) data accumulation time- the longer the accumulation time, the smaller the statistical error bars in the $A_2G_2(t)$.

ii) fractional weight of a sites i - If fi is smaller than 10% not much faith is put in the fits unless they are reproducible.

iii) line broadening - changes in the line broadening δi can effect the fraction and frequencies and therefore the fit as a whole.

iv) the right model - If the probe in the sample experiences a dynamical instead of a static interaction, a line broadening at that site can be the consequence in the fit. In our case we find the $A_2G_2(t)$ data of fraction f_1 appear to be damped at 500°C and even more at 600°C. Since a model for fluctuating field gradients between a and b axes is not yet ready, fits at 500°C and 600°C show a disproportionally large delta value, which is probably due to the dynamic fluctuations we have neglected.

v) known PAC frequencies - The PAC frequencies of the 211 phase are known accurately [54] and were not treated as variable fitting parameters in cases where such procedures could improve the accuracy of other parameters substantially

7.1.2. Summary of the measured and deduced PAC parameters

Using the fitting procedure described above, the PAC parameters for a sample with a high amount of ^{111}In dissolved in $YBa_2Cu_3O_{7-x}$ were deduced. The accumulation time for each run was a little short, but that made it possible to go thru a temperature range from 23° to 1060°C, including two cycles for checking the reversibility of the orthorhombic to tetragonal phase transition. The data were taken in an atmosphere of flowing oxygen and the sample was contained in an alumina sample holder. The parameters found are displayed in the order in which the points were measured in table 7.1. The errors in η and Vzz(lat) have been calculated in the following manner :

From the fitted value, let's say $\omega 1=40.6$ and $\omega 2=72.1$, $\eta=0.32$ and $Vzz=0.63$ are calculated. To account for the statistical errors in ω_1 and ω_2, two other values for eta and Vzz are calculated in using the error extrems of $\omega 1$ and $\omega 2$, what would be in this example :

(i) $\omega_{1new}=\omega_1+.5$, $\omega_{2new}=\omega_2-1.2$ and

(ii) $\omega_{1new}=\omega_1-.5$, $\omega_{2new}=\omega_2+1.2$.

The resulting different values for η and Vzz were compared with the above ones and the maximum deviation was used to account for the statistical errors in η and Vzz.

Table 7.1 PAC parameters from a 123 sample obtained between room temperature and 1060°C. The data are presented in the order in which the points were measured. ( ) refer to the statistical errors of the parameters found by the fitting program and the procedure described above. Numbers without ( ) were set constant in the fit.

f_i	ω_1	ω_2	δ	η	Vzz[lat]	T
[%]	[10^{-6} rad/sec]		[%]		[10^{-16} V/cm^2]	[°C]
f1 70(8)	40.6(5)	72.1(12)	5(2)	0.32(5)	0.63(1)	23
f4 12(3)	149.5(47)	255.7(81)	2	0.37(9)	2.28(7)	
f7 18	57.5	102.5	8	0.31	0.90	
f1 68(5)	39.0(4)	67.9(8)	4(1)	0.35(5)	0.60(1)	200
f4 12(2)	140.5(36)	240.7(65)	2	0.37(8)	2.14(4)	
f7 20	57	105	5	0.26	0.92	
f1 72(6)	31.5(6)	50.5(10)	6(2)	0.45(5)	0.45(1)	600
f4 12(3)	136.6(47)	258.0(81)	2	0.21(21)	2.26(6)	
f7 18	55.5	103	2	0.25	0.90	
f2 70(3)	17.0(6)	32.7(10)	0	0.18(18)	0.28(1)	700
f4 13(3)	142.3(35)	268.0(71)	2	0.22(13)	2.20(18)	
f7 17	55	102.5	2	0.24	0.90	
f1 77(6)	38.9(4)	65.2(7)	4(1)	0.40(3)	0.58(1)	250
f4 12(2)	142.0(35)	241.0(59)	2	0.38(7)	2.15(5)	
f7 11	57	105	5	0.26	0.92	
f2 76(2)	17.9(4)	33.9(7)	0	0.21(12)	0.29(1)	700
f4 14(2)	134.1(28)	262.6(9)	2	0.13(12)	2.29(2)	
f7 18	55	102.5	2	0.24	0.90	

f_i [%]	ω_1 [10^{-6} rad/sec]	ω_2	δ [%]	η	Vzz[lat] [10^{-16} V/cm^2]	T [°C]
f2 73(2)	16.9(5)	32.8(8)	0	0.15(15)	0.28(1)	800
f5 15(2)	136.6(36)	273.2	2	0.0	2.38(8)	
f7 12	54.4	101.5	2	0.24	0.89	
f2 72(2)	17.0(4)	32.1(8)	0	0.22(14)	0.28(1)	900
f5 17(2)	138.6(22)	277.2	2	0	2.41(6)	
f 7 11	54	100	2	0.25	0.88	
f2 71(2)	17.5(3)	33.6(5)	0	0.18(10)	0.29(1)	950
f5 22(1)	140.5(2)	281.0	2	0.0	2.44(2)	
f7 7	53	100	2	0.22	0.87	
f1 73(5)	39.5(5)	66.3(10)	6(1)	0.40(4)	0.59(1)	220
f4 11(3)	146.0(38)	246.4(67)	2	0.39(8)	2.20(5)	
f7 16	57	105	5	0.26	0.92	
f2 49(2)	16.5(4)	31.4(8)	0	0.20(20)	0.27(1)	970
f3 17(1)	0	0	0	0	0	
f5 24(2)	141.8(14)	283.6	2	0	2.46(4)	
f7 10	53	100	2	0.22	0.87	
f3 62(2)	0	0	0	0	0	1050
f7 27	53	98	2	0.25	0.86	
f8 11(2)	173(2)	339(4)	1	0.13(6)	2.95(8)	

Table 7.1 (continued)

With the help of table 7.1 the following information about the 123-system was deduced :

- A reversible structural change due to the orthorhombic to tetragonal phase transition was observed between 600° and 700°C. The two temperature cycles: 600°-700°-250°-700°C and 950°-220°-970°C showed that the PAC parameters of fraction f_1 and fraction f_2 are complementary spectra from the same site in different phases.
- A broadening of δ from fraction 1 with increasing temperature, indicating the insufficiency of the static interaction model. At the present time work is in progress to develop a model which would take care of the electric field gradient fluctuations due to the switching a- and b-axes as explained in chapter 2.
- An increase of fraction f_5 at temperatures closer to the melting point of 123 and its disappearance when the melting point of 123 is passed, strongly suggest that this is also a 123-site.
- A decrease in fraction f_2 happens at the same time when fraction f_5 increases, but the sum of f_2 and f_5 is constant within the uncertainties. Fraction f_2 also disappears at temperatures higher than the melting point.

Two more comments should be added :

i) For the site f_2 an eta of 0 is expected (symmetry of yttrium site in tetragonal phase), but systematic errors associated with the fitting of such a low frequency are large enough that the fitted non zero eta value is probably an experimental artifact. Further research with better time resolution and on samples with lesser second phase content should resolve that question.

ii) Experiments performed on other samples at different temperatures show that the phase transition takes place between 600° and 640°C.

Figure 7.1 shows four PAC time and Fourier spectra from the sample discussed in table 7.1 at 600°, 700°, 250° and 700°C. The spectra at 600° and 250° C are attributed to the orthorhombic phase, whereas the runs at 700°C refer to the tetragonal phase. The temperature cycle shows that the phase transition is reversible.

Figures 7.2 and 7.3 show the temperature dependence of the PAC parameters ω_1, ω_2, η and Vzz(lat) of the fractions f_1, f_2, f_4 and f_5 as obtained from table 7.1.

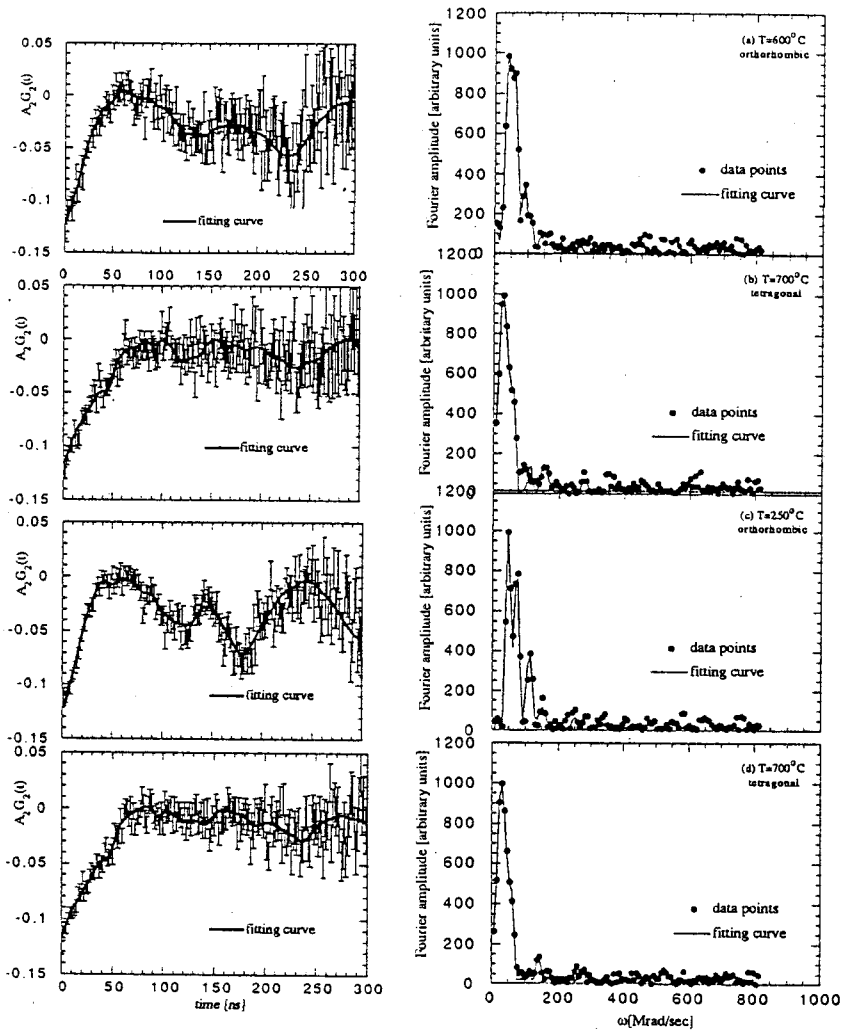

Fig. 7.1. $A_2G_2(t)$s and Fourier transforms of run number 3,4,5 and 6 from table 7.1 showing the reversibility of the orthorhombic to tetragonal phase transition. The cycle starts with the orthorhombic phase (a) at 600°C, transforms to the tetragonal phase (b) at 700°C, changes back to the orthorhombic phase at 250°C (c) and transforms again to the tetragonal phase at 700°C (d).

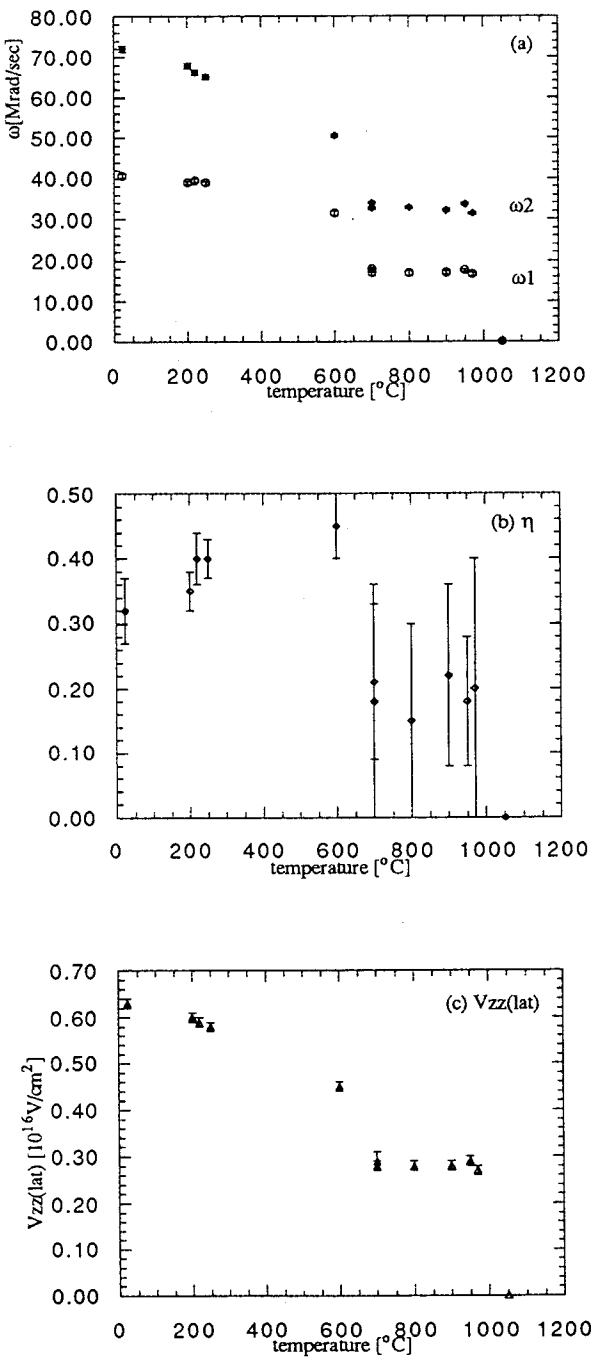

Fig. 7.2. Temperature dependence of (a) ω_1 and ω_2 , (b) η and (c) Vzz(lat) of fraction f_1 [23°-600°oC] and f_2[700°-970°C]

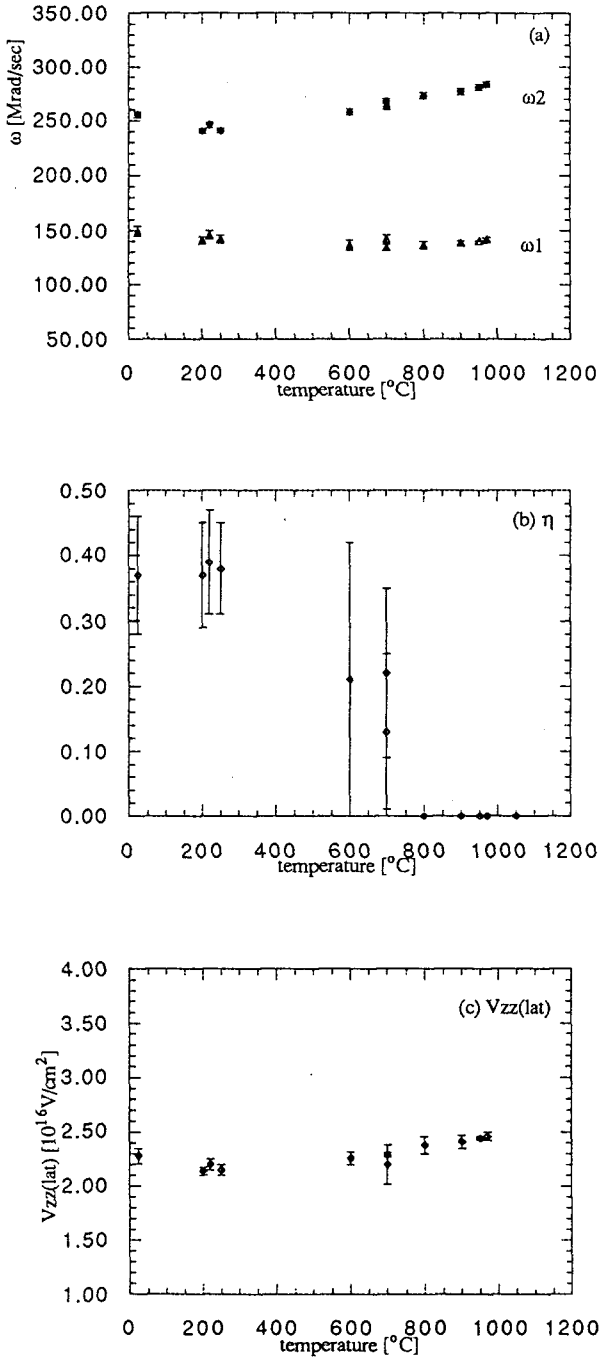

Fig. 7.3. Temperature dependence of (a) ω_1 and ω_2 , (b) η and (c) Vzz(lat) of fraction f_4 [23°-600°oC] and f_5[700°-970°C]

The results discussed next are from another sol gel prepared sample where the temperature range from 950° to 1050°C was investigated more carefully and in smaller temperature steps. This time the sample was contained in a MgO sample holder when it was exposed to an atmosphere of flowing oxygen. The accumulation time has been longer than in the sample discussed in table 7.1 and therefore shows better statistics. The PAC parameters are displayed in table 7.2.

Table 7.2. PAC parameters deduced from a sample which was held in an atmosphere of flowing oxygen at T=950°, 975°,985°,1015°, 1025° and 1050°C. The error bars in η and Vzz have been determined as described above. ( ) refer to the statistical error in the parameter found by the fitting program. Numbers without ( ) were set constant in the fit.

f_i	ω_1	ω_2	δ	η	Vzz[lat]	T
[%]	[10^{-6} rad/sec]		[%]		[10^{-16}V/cm^2]	[°C]
f_2 37.4(10)	16.2(4)	30.1(7)	0	0.25(11)	0.26(1)	950
f_5 25.6(13)	140.6(7)	281.2	2	0	2.44(3)	
f_6 15.4(17)	476(3)	746(7)	1	0.48(2)	6.76(9)	
f_7 21.6	54.6(7)	99.9(9)	1	0.27(1)	0.88(3)	
f_2 29.4(10)	16.0(4)	30.1(10)	0	0.16(16)	0.27(1)	975
f_5 31.3(13)	141.5(5)	283	2	0	2.46(2)	
f_6 20.4(18)	469(2)	798(6)	1	0.38(3)	7.12(8)	
f_7 18.9	55.4(7)	99.8(9)	1	0.30(2)	0.88(3)	
f_2 28.0(12)	15.5(7)	30.1(12)	0	0.15(15)	0.27(1)	985
f_5 29.4(15)	141.7(6)	283.4	2	0	2.46(2)	
f_6 20.3(21)	466(2)	795(6)	1	0.42(3)	6.87(8)	
f_7 22.3	55.6(7)	100.0(9)	1	0.27(2)	0.88(2)	

f_i	ω_1	ω_2	δ	η	Vzz[lat]	T
[%]	[10^{-6} rad/sec]		[%]		[10^{-16} V/cm^2]	[°C]
f_2 31.0(11)	16.0(7)	32.0(11)	0	0.00(25)	0.27(1)	1015
f_5 30.3(15)	142.4(6)	284.8	2	0	2.47(2)	
f_6 18.1(21)	463(3)	809(8)	1	0.34(2)	7.19(9)	
f_7 20.6	55.9(7)	100.5(8)	1	0.30(2)	0.88(2)	
f_2 26.3(11)	16.3(6)	30.1(10)	0	0.26(17)	0.26(1)	1025
f_5 35.2(15)	141.9(5)	283.8	2	0	2.46(2)	
f_6 20.1(19)	460(2)	809(6)	1	0.33(3)	7.18(9)	
f_7 20.6	55.9(7)	100.5(8)	1	0.30(2)	0.88(2)	
f_2 9.1(5)	16	31	0	0.16	0.27(1)	1050
f_3 44.5(3)	0	0	0	0	0	
f_5 9.7(6)	141.5	283	2	0	2.46(2)	
f_6 2.2(6)	465(11)	717(26)	1	0.5	6.51(9)	
f_7 34.5	54.4(2)	98.6(3)	1	0.29(1)	0.87(1)	

Table 7.2 (continued)

The last fit in table 7.2 has been made with $[\omega_1, \omega_2]$ of fractions f_2 and f_5 held constant . The data don't clearly display if there is any site of 123 left at this temperature. The fractions f_2 and f_5 are probably artifacts of the fit, since these sites don't appear naturally when the parameters $[\omega_1, \omega_2]$ are left as free variables. That means that the statistical errors in f_2 and f_5 are not well defined and definitely larger than indicated.

Figures 7.4 and 7.5 show the temperature dependence of the PAC parameters ω_1, ω_2, η and Vzz(lat) of fractions f_2 and f_5 as displayed in table 7.2.

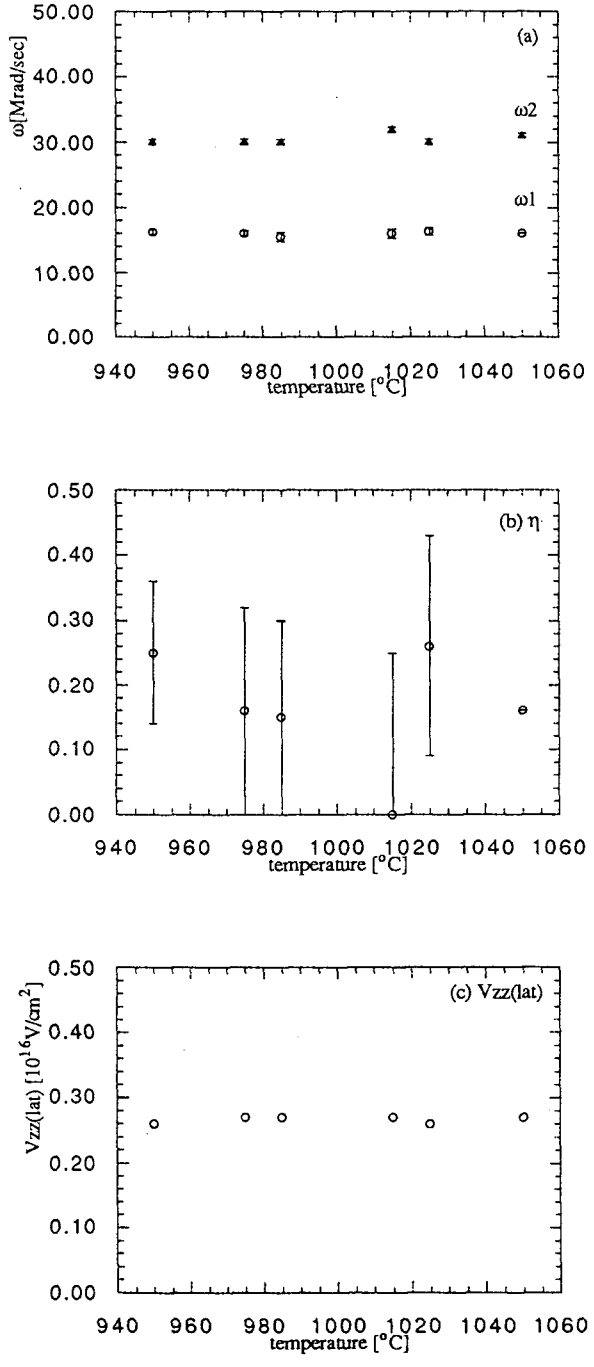

Fig. 7.4. Temperature dependence of (a) ω_1 and ω_2 , (b) η and (c) Vzz(lat) of fraction f_2

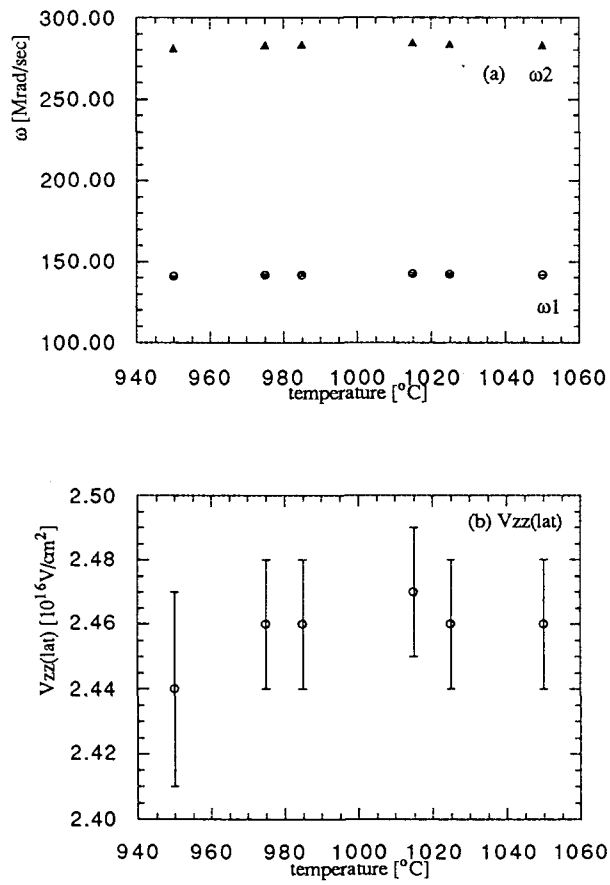

Fig. 7.5. Temperature dependence of (a) ω_1 and ω_2 and (b) Vzz(lat) of fraction f_5. η was held constant during the fits (η=0).

Several words of caution need to be said concerning the interpretation and validity of fraction f_6 in table 7.2. The Fourier spectra of this and other runs clearly show a peak for ω_1 at around 470 Mrad, but it is not yet clear where the corresponding second peak of ω_2 is. Due to limitations in the time resolution of our system the second peak is in its intensity too close to the background to be detected unambiguously. That has the effect that ω_2 values choosen at 650 Mrad or even at 940 Mrad result in similar fits. Runs made at temperatures above the melting point of 123 indicate that the ω_1=470 Mrad site also disappears with the other two 123-signals. More samples have to be investigated to resolve this question.

An interesting feature connected to the percentage weights of fractions f_2 and f_5 displays figure 7.6, showing that f_2 decreases from 37.4% at 950°C to 26.3% at 1025°C, whereas f_5 increases from 25.6% at 950°C to 35.2% at 1025°C, but finding the sum of f_2 and f_5 to be a constant between 950° and 1025°C. This result is interpreted as an evidence for a thermally populated copper site.

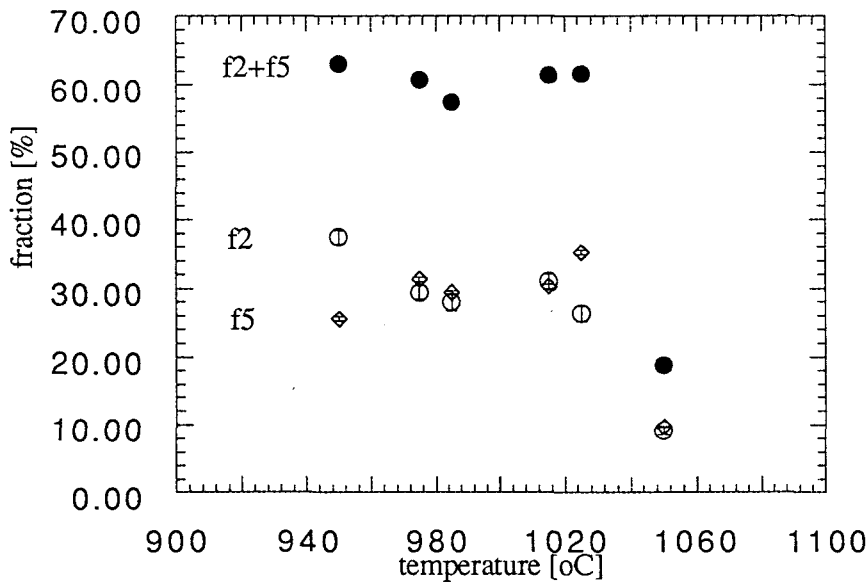

Fig. 7.6. (a) fraction f_2 versus temperature
(b) fraction f_5 versus temperature
(c) fraction $ft=f_2+f_5$ versus temperature

8. Discussion and conclusions

8.1. Comparison with other PAC results on 123

A good starting point for the discussion of the PAC parameters obtained in this work is made by asking how well they compare to PAC data found by other groups (see table 5.1 and 5.2). The only agreement is found in the assignment of fraction f_1 by Plank et al.[72]. They measured the parameters of f_1 in the temperature range from -248°C to +400°C and therefore overlap with our data only at three temperatures, namely 23°, 200° and 400°C. They mention that about 50% of their probe nuclei were exposed to this well defined field gradient.

None of the sites indicated by ω_1 being around 240 Mrad and η=1, as published by Uhrmacher et al. [70,71,80] and Singh et al. [73], have been found in the sol gel prepared samples, but they are not unknown to our group. This special frequency, named mystery phase by H.Su [54], has been seen when samples were prepared under reduced oxygen flow. In one of the samples prepared by the nitrate route, a site with frequency ω_1=235 and η=1 was observed at a temperature well above the melting point of 123 (1070°C). The 123 tetragonal phase fractions f_2 and f_5 had been melted away at 1070°C. Uhrmacher et al. [80] have identified a similar site in 202 (blue phase) and the most reasonable hypothesis consistent with all known data is that when this site is seen, it is ^{111}In in the 202 phase and not in 123.

8.2 Summary and conclusions

The microscopic structure of $YBa_2Cu_3O_{7-x}$ has been investigated between room temperature and 1050°C in an atmosphere of flowing oxygen using ^{111}In as a PAC tracer. Applying the sol gel preparation method, highly reproducible PAC spectra consisting of maximal five superimposed $A_2G_2(t)$s, were obtained and analyzed by the standard fitting model for static quadrupole interaction. The PAC probe proved to be sensitive to the well known orthorhombic to tetragonal phase

transition. Furthermore the observed PAC parameters display the expected behaviour at higher temperatures:

(i) a temperature dependent population of sites in 123, and

(ii) a disappearance of the 123 signals at T higher than the melting point of 123.

8.2.1 Phase transition

It was possible to reproduce the orthorhombic to tetragonal phase transition cyclically. The $A_2G_2(t)$ and its Fourier transform change drastically between 600° and 640°C without alternating the fractional weight associated with PAC parameters above and below the phase transition. This fractional weight is interpreted as ^{111}In substituted at the yttrium site experiencing two different electric environments. It should be mentioned that the PAC data indicate a phase transition temperature between 600° and 640°C, which is approximately 40°C below the one found by X-ray and neutron measurements. The reason for this behaviour lies in the different time scales of this two techniques. X-ray diffraction provides a fast, but spatial averaged spectrum, whereas PAC is a local probe whose time scale is of order nanoseconds. Since the phase transition is connected to a loss of oxygen, accompanied by fluctuating O(4) and O(5) sites, a PAC probe would distinguish between three temperature regimes:

(a) if T is low enough so that the switching time between a and b axes is small compared to the half-life of the intermediate state of the probe atom , a static quadrupole interaction pattern is expected.

(b) if T is high enough so that the switching time between a and b axes is large compared to the half-life of the intermediate state of the probe atom , an averaged static quadrupole interaction pattern with different PAC parameters is expected

(c) if T is in a range where switching time between a and b axes is comparable to the half-life of the intermediate state of the probe atom, a dynamic line-broadening is expected and has to be included in the model.

The measurement of a tetragonal site $A_2G_2(t)$ at 640°C indicates that the fluctuation rate is already sufficiently large to give an averaged electric field gradient. The diffraction measurements, being faster, still show an orthorhombic pattern.

8.2.2 Observations near and above the decomposition temperature of 123

PAC spectra measured at higher temperatures reveal a site f_5, which increases its weight as the temperature approaches the melting point of 123 and disappears above it. The tetragonal phase fraction f_2 decreases by the amount f_5 gains, so that the sum between f_5 and f_2 appears to be a constant and disappears when the melting point is passed. Site f_5 is interpreted to be a copper site whose population increases rapidly with temperature.

References

1. J. G. Bednorz and K. A. Müller, Z. Phys. B **64**, 189 (1986).

2. M. K. Wu et al., Phys. Rev. Lett. **58**, 908 (1987).

3. J. M. Tarascon et al., Phys. Rev. B **35**, 7115 (1987).

4. R. J. Cava et al., Rev. Lett. **58**, 1676 (1987)

5. Z. Z. Sheng and A. M. Hermann, Nature **332**, 138 (1988).

6. S.S. Parken et al. , Phys. Rev. Lett. **61**, 750 (1988).

7. R. J. Cava, Science ,Vol. **247**, 656 (1990).

8. R.J. Cava, Scientific American, **8**, 42 (1990)

9. R. Beyers, T.M. Shaw, Solid State Physics, Vol. **42**, 141 (1989)

10. J.D. Jorgensen et al., Phys. Rev. B **36**, 3608 (1987)

11. A.J.Vega et al., Phys. Rev. B **39**, 2322 (1989)

12. C.H.Chen et al., Phys. Rev. B **38**, 2888 (1988)

13. M.Alerio et al., Mater.Res.Soc. Symp. Proc.**99**, 41 (1988)

14. Y.Tokura et al., Nature, **337**, 345 (1989)

15. P.H. Hor et al., Phys.Rev.Lett. **58**, 1891 (1987)

16. T.Itoh et al., Phys.Lett.**A 129**, 67 (1988)

17. E.Specht.et al., Phys.Rev.B **37**, 7426 (1988)

18. J.D. Jorgensen et al., Phys. Rev. B **36**, 3608 (1987)

19. E.Specht.et al., Phys.Rev.B **37**, 7426 (1988)

20. S.Nakahara et al., J.Appl.Phys. **63**, No.2, 451 (1988)

21. C.J.Jou and J.Washburn, J.Mater.Res., Vol. **4**, No.4, 795, (1989)

22. O.R. Monterio, S. Johnson, J.Am.Ceram.Soc.,**73**, 1159 (1990)

23. Roth et al., Research Update, Ceramic Superconductors II, (1988)

24. T.Aselage and K.Keefer, J.Mater.Res., Vol. **3**, 1279 (1988)

25. A.Ono and T.Tanaka, Jpn.J.Appl.Phys. **26** (5), L825 (1987)

26. J.Takada et al., Jpn.J.Appl.Phys. **26** (10), L1707 (1987)

27. S. Holtzburg et al., Chemistry of High-Temperature Superconductors, ACS Symposium Series Vol.351, p.79 (1987)

28. S.Takekava and N.Iyi, Jpn.J.Appl.Phys. **26** (5), L851 (1987)

29. K.W.Lay and G.M. Renlund, J.Am.Ceram.Soc.,**73**, 1208 (1990)

30. P.K.Gallagher, Adv.Ceram.Mater., **2** [3B], 632 (1987)

31. M.Nevriva et al., Physica C, **153-155**, 377 (1988)

32. F.Greuter et al., Physica C, **153-155**, 361 (1988)

33. R.W. McCallum, J.Met., **41** [1], 50, (1989)

34. K.Frase et al., J.Am.Ceram.Soc., **70**, C-204 (1987)

35. Perturbed Angular Correlations, edited by E. Karlsson, E. Matthias, and K. Siegbahn, North–Holland, Amsterdam (1964).

36. E. Recknagel, G. Schatz, and Th. Wichert, in Hyperfine Interactions of Radioactive Nuclei, edited by J. Christiansen, – Verlag, Berlin (1983), pp. 133–204.

37. E. Recknagel, G. Schatz, and Th. Wichert, in Hyperfine Interactions of Radioactive Nuclei, edited by J. Christiansen, – Verlag, Berlin (1983), pp. 133–204.

38. G. S. Collins and R. B. Schuhmann, Phys. Rev. B **34**, 502 (1986).

39. H. Metzner, R. Sielemann, S. Klaumünzer, and E. Hunger, Phys.Rev. B **36**, 9535 (1987).

40. F. Raether, D. Wiarda, K. P. Lieb, J. Chevallier, and G. Weyer, Z. Phys. B **73**, 467 (1989).

41. W. Bolse, M. Uhrmacher, and K. P. Lieb, Phys. Rev. B **36**, 1818 (1987).

42. W. Segeth et al., Phys. Rev. B **39**, 10725, (1989).

43. A. F. Pasquevich and R. Vianden, Phys. Rev. B **35**, 1560 (1987).

44. A. F. Pasquevich and R. Vianden, Phys. Rev. B **37**, 10858 (1988).

45. K. Krusch and J. A. Gardner, Phys. Rev. B **24**, 4587 (1981).

46 M. Brüssler, H. Metzner, K.–D. Husemann, and H. J. Lewerenz, Phys. Rev. B **38**, 9268 (1988).

47. A. Lerf and T. Butz, Hyperfine Interactions **36**, 275 (1987).

48. R. Vianden, Hyperfine Interactions **15/16**, 1081 (1983).

49. H. Frauenfelder and R. M. Steffen, in Alpha– Beta– and Gamma–Ray Spectroscopy, Vol. 2, edited by K. Siegbahn, North–Holland, Amsterdam (1965), Chap. XIXA, pp997–1198.

50. B. Harmatz, Nuclear Data Sheets **27**, 453 (1979).

51. P. Herzog, K. Freitag, M. Reuschanbach, and H. Walitzki, Z. Phys. **A 294**, 13 (1980).

52. Table of Isotopes, 7/e, edited by C. M. Lederer and V. S. Shirley, Wiley–Interscience, New York (1978), p. 521.

53. H. Jaeger, Ph. D. Thesis, Oregon State University (1987), unpublished

54. H. Su, Ph. D. Thesis, Oregon State University (1989), unpublished

55. H. Fuchs, M.S. Thesis, Oregon State University (1990), unpublished

56. R. M. Steffen and K. Adler, in The Electromagnetic Interaction in Nuclear Spectroscopy, edited by W. D. Hamilton, North–Holland, Amsterdam (1975), Chap. 13, pp 583-643

57. A. Messiah, Quantum Mechanics, Vol. II, John Wiley & Sons, New York (1968)

58. E. Matthias, W. Schneider, and R. M. Steffen, Phys. Rev. **125**, 261 (1962).

59. J.M. Blatt and V.F.Weisskopf, Theoretical Nuclear Physics , Wiley, New York (1952)

60. E. Gerdau, J. Wolf, H. Winkler, and J. Braunsforth, Proc. R. Soc. A **311**, 197 (1969)

61 L. A. Mendoza–Zélis et al., Hyperfine Interactions **3**, 315 (1977).

62 A. Abragam and R. V. Pound, Phys. Rev. **92**, 943 (1953)

63 H. Jaeger, J. A. Gardner, H. T. Su and R. L. Rasera, Rev. Sci. Instrum. **58**, 1694 (1987).

64. A. R. Arends, C. Hohenemser, F. Pleiter, H. De Waard, L. Chow, and R. M. Sutter, Hyperfine Interactions **8**, 191 (1980).

65. P. R. Bevington, Data Reduction and Error Analysis for the Physical Sciences, McGraw–Hill, New York, (1969).

66 E.N. Kaufman R.J.Vianden, Rev.Mod.Phys.**51**, 161 (1979)

67. F. D. Feiock and W. R. Johnson, Phys. Rev. **187**, 39 (1969)

68. A. Baudry, P. Boyer, and P. Vulliet, Hyperfine Interactions **13**, 263 (1983).

69. P. C. Lopiparo and R. L. Rasera, in Angular Correlations in Nuclear Disintegration, edited by H. V. Krugten and B. Van Nooijen, Rotterdam University Press, Rotterdam (1971).

70. M.Uhrmacher et al., Phys.Lett.**A 142**, 181 (1989)

71. M.Uhrmacher et al.,J.Less-Common Met. **150**, 185 (1989)

72. H.Plank et al., Phys.Lett.**A 133**, 451 (1988)

73. P.Singh et al., Phys.Rev.B **39**, 2308 (1989)

74. S.Fries and F.Fraga : to be published on the proceedings of the Latin-American Conference on High Temp. Superconductivity

75. G.Catchen et al., Phys.Rev.B **38**, 2824 (1988)

76. W.Shen et al., Solid State Commun. **69**, 517 (1989)

77. Z.Akselrod et al., Hyperfine Interaction Conference Prag (1989)

78. A.Biblioni et al., Phys.Rev.B **32**, 2393 (1985)

79. A.Biblioni et al., Phys.Rev.B **37**, 4743 (1988)

80. M.Uhrmacher and M.Bartos, Zakopane Winter School (1989)

81. J.Fransaer et al., J.Appl.Phys. **65** , 3277 (1989)

82. B.Dunn et al., Adv.Ceram.Mater., **Vol 2**, No.3B, 344 (1987)

83. G.Weidlich, J.Gardner and J.Sommers, unpublished

84. R.Suryanarayanah et al., Physica C **153-155**, 874 (1988)

85. A.K.Bhattacharja and K.K.Singh, Physics C **152**, 283 (1988)